universität wien

MASTERARBEIT / MASTER'S THESIS

Titel der Masterarbeit / Title of the Master's Thesis

„Hydrogen Hyperfine Structure Measurements using the σ_1- and π_1-Transitions: Evaluation & Correction“

verfasst von / submitted by

Andreas Lanz, BSc

angestrebter akademischer Grad / in partial fulfilment of the requirements for the degree of

Master of Science (MSc)

Wien, 2019 / Vienna, 2019

Studienkennzahl lt. Studienblatt / degree programme code as it appears on the student record sheet:	UA 066 876
Studienrichtung lt. Studienblatt / degree programme as it appears on the student record sheet:	Masterstudium Physik
Betreut von / Supervisor:	Hon.-Prof. Dipl.-Phys. Dr. Eberhard Widmann
Mitbetreut von / Co-Supervisor:	

Abstract

The ASACUSA collaboration at CERN proposed an antihydrogen ground-state hyperfine transition measurement to test the CPT theorem. The experimental setup is tested with hydrogen. The transitions used for this experiment are the σ_1- and the π_1-transition. Therefore a spin-flip cavity was built capable of driving both transitions by a specific alignment of the static and oscillating magnetic fields.

The first part of this thesis deals with the evaluation of the data measured in 2017. One half of these data have already been evaluated in 2017 with MatLab. The evaluation is now repeated with ROOT to see if the achievable precision and final results are independent of the used software. The second half of the data have been evaluated in the present work for the first time. These data were measured at lower magnetic fields to get better extrapolation results by having more data points close to the interesting zero magnetic field region. The evaluation showed a deviation from the literature value at these points.

At low static magnetic field the σ_1- and the π_1-transition have almost the same frequency and interfere with each other, which changes the line-shape of the transition probability. In consequence the formerly used fit, based on a two-level simulation, does not yield accurate results. Solving a four-level system and calculating the difference from the transition frequency resulting from the two-level fit is applied to the data as a correction, which is done in the second part of this thesis. At the lower magnetic field region all transitions have to be taken into account and therefore, to get a more accurate result, the four-level system has to be solved.

Zusammenfassung

Die ASACUSA Kollaboration am CERN schlug eine Messung der Hyperfeinstruktur von Antiwasserstoff im Grundzustand vor, um das CPT Theorem zu testen. Der Aufbau des Experiments wird mit Wasserstoff getestet. Die Übergänge, welche dafür benutzt werden sollen, sind der σ_1- und der π_1-Übergang. Zu diesem Zweck wurde eine Spin-Flip Kavität gebaut, welche durch eine konkrete Ausrichtung des statischen und des oszillierenden Magnetfeldes imstande ist, beide Übergänge zu treiben.

Der erste Teil dieser Arbeit beschäftigt sich mit der Auswertung von Daten, welche 2017 gemessen wurde. Eine Hälfte der Daten wurde bereits 2017 mittels MatLab ausgewertet. Die Auswertung wird nun mit ROOT wiederholt, um zu sehen, ob die erreichbare Präzission und das Endergebnis unabhängig von der benutzten Software ist. Die zweite Hälfte der Daten wurde in dieser Arbeit zum ersten Mal ausgewertet. Diese Daten wurden bei kleinem Magnetfeld gemessen, da dadurch ein besseres Ergebnis mittels Extrapolation erreicht werden könnte, da mehr Datenpunkte im Bereich um den Nullpunkt des Magnetfeldes gemessen wurden. Die Auswertung zeigte eine Abweichung vom Literaturwert bei diesen Punkten.

Bei kleinem statischen Magnetfeld haben der σ_1- und der π_1-Übergang nahezu die gleiche Übergangsfrequenz und interferieren miteinander, was eine Änderung der Kurvenform der Übergangswahrscheinlichkeit bewirkt. Als Folge dieser Änderung, führt der zuvor benutzte Fit, welcher auf einem Zwei-Level System beruht, nicht mehr zu akkuraten Ergebnissen. Im zweiten Teil dieser Arbeit wird ein Vier-Level System gelöst und die Differenz dieser Übergangsfrequenz von der durch den Zwei-Level System Fit berechneten Übergangsfrequenz berechnet als Korrektur auf die Daten angewendet. Bei kleinem Magnetfeld müssen alle Übergänge beachtet werden und somit, für ein akkurates Ergebnis, das Vier-Level System gelöst werden.

Acknowledgement

At first I want to thank my parents Walter and Josefine Lanz. Without their support it would not have been possible for me to focus on my studies. Further I want to thank professor Eberhard Widmann for giving me the chance to be part of an international collaboration and the chance to participate in a really interesting experiment and for supervising this thesis.

The next person I want to thank is Dr. Martin Simon always taking the time to remove ambiguities and being patient with me. Without his support I would not have been able to finish this work.

Last but not least I want to thank all my colleagues at SMI for making the time memorable, the colleagues of the ASACUSA collaboration for being positively received and all the people from the University of Vienna who helped me during my thesis.

Contents

Chapter 1

Introduction

In particle physics the standard model (SM) explains processes and their underlying fundamental forces. It could predict particles - for example the Ω^- particle - and some properties of them. One important prediction was the existence of so-called antiparticles [1]. By solving the Dirac equation one gets two energy solutions: one positive and one negative. The antiparticles are described mathematically as the states of negative energy. Every particle has its corresponding antiparticle with exactly the same properties but different inner quantum numbers and sign of the charge. After the discovery of the positron in 1932 [2] the interest in antimatter rose.

With the observation of several antiparticles the idea of antielements, which are elements in which the nuclides and electrons are exchanged with the antiparticles, was proposed. In 1996 the first antihydrogen, the simplest antielement, was detected by the group PS210 at LEAR at CERN [3]. All together 11 antihydrogen events were observed. In 1997 the ASACUSA collaboration (Atomic Spectroscopy And Collisions Using Slow Antiprotons) proposed a technique to measure the ground-state hyperfine structure of antihydrogen in an antihydrogen beam [4]. To produce the antihydrogen the antiprotons are guided to a cloud of positrons. Using a Rabi-experimental setup it is a promising method to test the CPT invariance more precisely on an absolute scale than the experiments using the 1s-2s transition. A detailed description of the setup and the production of antihydrogen can be for example found in [5].

As it is quite difficult to produce an antihydrogen beam, which was achieved in 2014 [6], the experimental beamline is tested by using hydrogen. Hydrogen can be produced in a big amount without any big effort and therefore is ideal to characterise the experimental setup. By measuring the ground-state hyperfine structure of hydrogen, which is for hydrogen one of the best known values in physics, and comparing it with the one of antihydrogen, possible deviations can be observed. If there are any differences it would imply to reach new physics beyond the SM. One so-called Standard Model Extension (SME) is proposed by Kostelecký et al. [7] in which differences are allowed. The ASACUSA collaboration tries to verify this possible SME.

Former tests of the hydrogen beam apparatus measuring the π_1- and σ_1 transition

show that the experimental method works [8–10]. New data showed differences between the experimental results and the theory because the evaluation was done by using an approximated theory. Investigating the underlying theory and correcting the data, which is done in this thesis, shows some effects which have to be taken into concern when measuring the hyperfine transition of antihydrogen.

Chapter 2

Theory

2.1 CPT Theorem

In the SM symmetries are very important. They are directly connected to conservation laws and often can make theories simpler and more beautiful. There are two different types of symmetries: discrete and continuous. Continuous symmetries are for example spatial translation and time translation the so-called Lorentz boosts, an example for a discrete symmetry is parity.

Looking at particle interactions one can always ask the question which change in condition would let the process unaltered. The first believe was that physical processes are invariant under the so-called parity transformation - spatial inversion ($P(\vec{x}) \rightarrow -\vec{x}$) - as well as charge conjugation - inversion of all internal quantum numbers ($C\,|\psi\rangle = |\overline{\psi}\rangle$) and time reversal ($T(t) \rightarrow -t$). In strong and electromagnetic interactions this is true but for weak interactions it was measured by Wu et al. [11] that parity is broken by investigating the process

$$^{60}Co \rightarrow ^{60} Ni + e + \overline{\nu}_e \tag{2.1}$$

Charge conjugation can not be invariant in any process where neutrinos occur, because it would change a left-handed neutrino into a left-handed antineutrino which has not been detected at all. It was proposed that the invariance could be restored by seeing charge conjugation and parity as one combined symmetry. For the strong and electromagnetic interaction the combined transformation is invariant but it is broken in weak interactions. This was found by Cronin and Fitch investigating the decay paths of the neutral Kaon [12].

In quantum field theory of local fields CPT invariance - the simultaneous operation of charge conjugation, parity transformation and time reversal - is one of the most important principles [13]. One implication of the CPT theorem is that a particle and its antiparticle must have exactly the same mass and lifetime and have electric charge and magnetic moments which are equal in magnitude [14]. If CPT is invariant, time reversal has to be broken as strong as CP to compensate it in weak interactions.

2.2 The energy spectrum of the hydrogen atom

The hydrogen atom is the simplest atom and consists of an electron and a proton. Because of that it gained always special focus by physicists to understand and describe fundamental properties of elements. This section will concentrate on the analysis of the energy spectrum of hydrogen.

2.2.1 Fine structure

The study of the energy spectrum of hydrogen started with Niels Bohr's suggestion that the electron can only inhabit specific descrete orbitals with quantized angular momentum as integer multiples (principal quantum number n) of $\hbar = \frac{h}{2\pi}$ [15]. With this assumption he could predict the energy spectrum of the hydrogen atom rather precisely.

Going to a quantum mechanical calculation one has to solve the Schrödinger equation

$$\hat{H}\Psi(\vec{r},t) = i\hbar\frac{\partial\Psi(\vec{r},t)}{\partial t}\,, \tag{2.2}$$

but as the Schrödinger equation is a non-relativistic equation the solution must be corrected. To get a full relativistic and quantum-mechanical theory the Dirac equation [16]

$$(c\vec{\alpha}\cdot\vec{p}) + \beta mc^2 - V(\vec{r}))\psi = E\psi \tag{2.3}$$

has to be solved. In the Dirac equation c is the speed of light, ψ is a four-component spinor, m is the reduced mass of hydrogen, $V(\vec{r})$ is the potential, E the energy and β and the vector $\vec{\alpha}$ are dimensionless coefficients which in the standard representation are expressed through the Pauli matrices

$$\alpha_x = \begin{pmatrix} 0 & \hat{\sigma}_x \\ \hat{\sigma}_x & 0 \end{pmatrix},\ \alpha_y = \begin{pmatrix} 0 & \hat{\sigma}_y \\ \hat{\sigma}_y & 0 \end{pmatrix},\ \alpha_z = \begin{pmatrix} 0 & \hat{\sigma}_z \\ \hat{\sigma}_z & 0 \end{pmatrix},\ \beta = \begin{pmatrix} 1 & 0 \\ 0 & -1 \end{pmatrix} \tag{2.4}$$

where every component is a 2x2 matrix resulting in 4x4 matrices for $\vec{\alpha}$ and β. Inserting these matrices into eq. 2.3 and rewriting the four-component spinor as

$$\psi = \begin{pmatrix} \psi_A \\ \psi_B \end{pmatrix},\ \text{with}\ \psi_A = \begin{pmatrix} \psi_1 \\ \psi_2 \end{pmatrix}\ \text{and}\ \psi_B = \begin{pmatrix} \psi_3 \\ \psi_4 \end{pmatrix} \tag{2.5}$$

leads to two equations for the two-component spinors

$$\hat{\vec{\sigma}} \cdot \hat{\vec{p}} \psi_B = \frac{1}{c}(E - V(\vec{r}) - mc^2)\psi_A \tag{2.6}$$

$$\hat{\vec{\sigma}} \cdot \hat{\vec{p}} \psi_A = \frac{1}{c}(E - V(\vec{r}) + mc^2)\psi_B \tag{2.7}$$

For hydrogen the potential is $V(r) = -\frac{e^2}{r}$ which is radially and therefore the radial and the angular motion can be separated in these two equations.

Thus the generalised spherical harmonics[1] can be used for the ansatz

$$\psi_A = \frac{F(r)}{r}\mathcal{Y}_{j,m,l_A}, \quad \psi_B = i\frac{G(r)}{r}\mathcal{Y}_{j,m,lB} \tag{2.8}$$

By using the identity

$$\hat{\vec{\sigma}} \cdot \hat{\vec{p}} = \frac{1}{r^2}\hat{\vec{\sigma}} \cdot \vec{r}\left(\frac{\hbar}{i} r \frac{\partial}{\partial r} + i\hat{\vec{\sigma}} \cdot \hat{\vec{L}}\right) , \tag{2.9}$$

where $\hat{\vec{L}}$ is the orbital angular momentum, and the properties

$$\frac{1}{r}(\hat{\vec{\sigma}} \cdot \vec{r})\mathcal{Y}_{j,m,l=j+1/2} = -\mathcal{Y}_{j,m,l=j-1/2} \tag{2.10}$$

$$\frac{1}{r}(\hat{\vec{\sigma}} \cdot \vec{r})\mathcal{Y}_{j,m,l=j-1/2} = -\mathcal{Y}_{j,m,l=j+1/2} \tag{2.11}$$

the radial Dirac equation for the radial wave functions $F(r)$ and $G(r)$ can be derived

$$\hbar c\left(\frac{dF}{dr} + \frac{\kappa}{r}F\right) = (E + \frac{e^2}{r^2} + mc^2)G \tag{2.12}$$

$$\hbar c\left(\frac{dG}{dr} - \frac{\kappa}{r}G\right) = (E + \frac{e^2}{r^2} + mc^2)F \tag{2.13}$$

with κ is

$$-j - \frac{1}{2} \quad \text{for} \quad l_A = j - \frac{1}{2},\ l_B = j + \frac{1}{2} \tag{2.14}$$

$$j + \frac{1}{2} \quad \text{for} \quad l_A = j + \frac{1}{2},\ l_B = j - \frac{1}{2} \tag{2.15}$$

[1] Generalised spherical harmonics [16]:

$$\mathcal{Y}_{j,m,l} = \frac{1}{\sqrt{2j}}\begin{pmatrix}\sqrt{j+m}Y_{l,m-\frac{1}{2}}(\theta,\phi)\\ \sqrt{j-m}Y_{l,m+\frac{1}{2}}(\theta,\phi)\end{pmatrix} \quad for \quad j = l + \frac{1}{2}$$

$$\mathcal{Y}_{j,m,l} = \frac{1}{\sqrt{2j+2}}\begin{pmatrix}-\sqrt{j+1-m}Y_{l,m-\frac{1}{2}}(\theta,\phi)\\ \sqrt{j+1+m}Y_{l,m+\frac{1}{2}}(\theta,\phi)\end{pmatrix} \quad for \quad j = l - \frac{1}{2} ,$$

with $Y_{l,m}(\theta,\phi)$ are the spherical harmonics

Solving these two differential equations the fine structure energy levels result in

$$E_{n,j} = mc^2 \left[1 + \frac{\alpha^2}{\left(n - j - \frac{1}{2} + \sqrt{(j+\frac{1}{2})^2 - \alpha^2} \right)^2} \right]^{-\frac{1}{2}} \tag{2.16}$$

with $\alpha = \frac{e^2}{\hbar c}$ is the fine structure constant characterising the strength of the electromagnetic interaction, n is the principal quantum number and j is the total angular momentum quantum number.

The Dirac equation still deviates from measurements. Going to a quantumelectrodynamical (QED) derivation the self-energy of the electron and the vacuumpolarisation additionally play roles. A derivation of this so-called Lamb-shift would go beyond the scope of this thesis but can be found in [17]. Therefore just the resulting shift of the energy levels from the calculation by the Dirac equation is shown here

$$\Delta E = \frac{8\alpha^3}{3\pi} \frac{1}{n^3} \mathrm{Ry} \left[\log \left(\frac{mc^2}{2(E - E_0)_{\mathrm{avg}}} \right) + \frac{5}{6} - \frac{1}{5} \right] \qquad \text{for} \quad l = 0 \tag{2.17}$$

$$\Delta E = \frac{\alpha^3}{2\pi} \frac{1}{n^3} \mathrm{Ry} \frac{1}{(l+\frac{1}{2})(l+1)} \qquad \text{for} \quad j = l + \frac{1}{2} \tag{2.18}$$

$$\Delta E = -\frac{\alpha^3}{2\pi} \frac{1}{n^3} \mathrm{Ry} \frac{1}{l(l+\frac{1}{2})} \qquad \text{for} \quad j = l - \frac{1}{2} \tag{2.19}$$

with $\mathrm{Ry} = \frac{e^4 m}{32\pi^2\hbar^4} = 13.6056\,\mathrm{eV}$ is the Rydberg energy unit and E_0 is the ground-state energy and $(E - E_0)_{\mathrm{avg}}$ is defined by

$$\sum_n (E_n - E_0) \left| \vec{p}_{n0} \right|^2 \log |E_n - E_0| = \left[\sum_n (E_n - E_0) \left| \vec{p}_{n0} \right|^2 \right] \log (E - E_0)_{\mathrm{avg}} \tag{2.20}$$

2.2.2 Hyperfine Structure

Going deeper into the discussion of the energy spectrum of the hydrogen atom and taking the magnetic interaction between the electron shell with the atomic nucleus one gets to an even smaller splitting of the energy levels - the so-called hyperfine structure. In this chapter only the most important steps of the calculation are presented, a more detailed derivation of the hyperfine structure is given in Ref. [8], [9] and [18].

The hydrogen atom consists of an electron and a proton. As both particles are spin-1/2 particles there are 4 possible orientations

$$\text{State 1}: \quad |{+}{+}\rangle$$
$$\text{State 2}: \quad |{+}{-}\rangle$$
$$\text{State 3}: \quad |{-}{+}\rangle$$
$$\text{State 4}: \quad |{-}{-}\rangle$$

where the first sign in the ket labels the electron spin and the second one the proton spin. "+" means spin up and "−" means spin down for example $|{+}{-}\rangle$ stands for electron spin up and proton spin down. An arbitrary state can be written as a superposition of the base states with complex coefficients C_i (i=1,2,3 or 4)

$$|\psi\rangle = C_1 |{+}{+}\rangle + C_2 |{+}{-}\rangle + C_3 |{-}{+}\rangle + C_4 |{-}{-}\rangle \tag{2.21}$$

Following the arguments in [18] the Hamiltonian of the hydrogen atom is

$$\hat{H} = E_0 \cdot \hat{I} + A \cdot \hat{\vec{S}}^e \cdot \hat{\vec{S}}^p \tag{2.22}$$

with $\hat{\vec{S}}^e = \frac{\hbar}{2}\vec{\sigma}^e$ is the spin operator of the electron, acting only on the electron spin, and similarly $\hat{\vec{S}}^p$ for the proton. The zero point energy E_0 can be chosen arbitrarily, so in this work it will be set to zero. $\hat{I}$ is the identity and A is a constant which has to be calculated. The next step is to solve the Schrödinger equation (2.2) which can be written in the form

$$i\hbar\dot{C}_i = H_{ij}C^j \tag{2.23}$$

With the spin operators acting on the states given in table 2.1 the matrix elements $\langle i|\,\hat{H}\,|j\rangle = H_{ij}$ can be calculated to

$$H = \begin{pmatrix} A & 0 & 0 & 0 \\ 0 & -A & 2A & 0 \\ 0 & 2A & -A & 0 \\ 0 & 0 & 0 & A \end{pmatrix} \tag{2.24}$$

Table 2.1: Acting of the sigma matrices on the base vectors.

$\sigma_x \|{+}\rangle = +\|{-}\rangle$
$\sigma_x \|{-}\rangle = +\|{+}\rangle$
$\sigma_y \|{+}\rangle = +i\|{-}\rangle$
$\sigma_y \|{-}\rangle = -i\|{+}\rangle$
$\sigma_z \|{+}\rangle = +\|{+}\rangle$
$\sigma_z \|{-}\rangle = -\|{-}\rangle$

Inserting the Hamiltonian in eq. (2.23) yields four differential equations

$$i\hbar\dot{C}_1 = AC_1 \tag{2.25}$$
$$i\hbar\dot{C}_2 = -AC_2 + 2AC_3 \tag{2.26}$$
$$i\hbar\dot{C}_3 = 2AC_2 - AC_3 \tag{2.27}$$
$$i\hbar\dot{C}_4 = AC_4 \tag{2.28}$$

which can be solved using the ansatz $C_i = a_i e^{-\frac{i}{\hbar}Et}$. This will lead to four final states [9]

$$|1\rangle = |{+}{+}\rangle \qquad \text{with } E_1 = A \tag{2.29}$$
$$|2\rangle = \frac{1}{\sqrt{2}}\big(|{+}{-}\rangle + |{-}{+}\rangle\big) \qquad \text{with } E_2 = A \tag{2.30}$$
$$|3\rangle = |{-}{-}\rangle \qquad \text{with } E_3 = A \tag{2.31}$$
$$|4\rangle = \frac{1}{\sqrt{2}}\big(-|{+}{-}\rangle + |{-}{+}\rangle\big) \qquad \text{with } E_4 = -3A \tag{2.32}$$

where $\frac{1}{\sqrt{2}}$ is for normalizing. As it can be seen there is a triplet state with energy $E_1 = A$ and a singlet state with $E_4 = -3A$. One can further investigate the Zeeman splitting, which is the change of the states in an external magnetic field. The energy of an electron (or proton) in an external magnetic field $\vec{B}$ if it was alone is $-\vec{\mu}\cdot\vec{B}$. Therefore the Hamiltonian changes to

$$\hat{H} = A(\hat{S}^e \cdot \hat{S}^p) - \vec{\mu}_e \cdot \vec{B} - \vec{\mu}_p \cdot \vec{B} \tag{2.33}$$

where $\vec{\mu}_e = \frac{\mu_\mathrm{B} g_I}{\hbar}\hat{S}^e$ and $\vec{\mu}_p = \frac{\mu_\mathrm{B} g_J}{\hbar}\hat{S}^p$ are the magnetic moments of the electron and the proton respectively, μ_B is the Bohr magneton and g_I and g_J are the Landé factors of the orbit and the nucleus. The first term of the Hamiltonian is the unperturbed part which was solved before. Repeating the calculation above with the second two terms and set $\vec{B} = B\vec{e}_z$ one gets a final Hamiltonian [8]

$$H^\mathrm{f} = \begin{pmatrix} A-(\mu_J+\mu_I)B & 0 & 0 & 0 \\ 0 & -A-(\mu_J-\mu_I)B & 2A & 0 \\ 0 & 2A & -A+(\mu_J-\mu_I)B & 0 \\ 0 & 0 & 0 & A+(\mu_J+\mu_I) \end{pmatrix} \tag{2.34}$$

with $\mu_I = \frac{g_I\mu_\mathrm{B}}{2}$ and $\mu_J = \frac{g_J\mu_\mathrm{B}}{2}$. The eigenvalue problem with this final Hamiltonian leads to four equations which have to be solved

$$Ea_1 = (A + \mu B)a_1 \tag{2.35}$$
$$Ea_2 = (-A + \mu' B)a_2 + 2Aa_3 \tag{2.36}$$
$$Ea_3 = (-A - \mu' B)a_3 + 2Aa_2 \tag{2.37}$$
$$Ea_4 = (A - \mu B)a_4 \tag{2.38}$$

where $\mu = -(\mu_J + \mu_I)$ and $\mu' = -(\mu_J - \mu_I)$. Equation (2.35) and (2.38) depend just on one coefficient, therefore the solutions are

$$E_1 = A + \mu B \quad \text{with} \;\; a_1 = 1, \;\; a_2 = a_3 = a_4 = 0 \tag{2.39}$$
$$E_3 = A - \mu B \quad \text{with} \;\; a_1 = a_2 = a_3 = 0, \;\; a_4 = 1 \tag{2.40}$$

The other two equations have to be solved simultaneously to get the energies [9]

$$E_2 = -A + \sqrt{\mu'^2 B^2 + 4A^2} \tag{2.41}$$
$$E_4 = -A - \sqrt{\mu'^2 B^2 + 4A^2} \tag{2.42}$$

With these energies the ratio

$$\frac{a_2}{a_3} = \frac{E_2 + A + \mu' B}{2A} = \sqrt{1 + \left(\frac{\mu' B}{2A}\right)} + \frac{\mu' B}{2A} \tag{2.43}$$

follows and with the ansatz $a_2 = \cos\theta$ & $a_3 = \sin\theta$ having the mixing angle

$$\theta = \arctan\left(\frac{1}{\sqrt{1 + x^2} + x}\right) \tag{2.44}$$

with $x = \frac{B}{B_C}$ and $B_C = \frac{2A}{\mu'}$. Using the ansatz $a_2 = -\sin\theta$ and $a_3 = \cos\theta$ for the energy E_4 leads to the eigenstates of the mixed states

$$|2\rangle = \cos\theta\,|+-\rangle + \sin\theta\,|-+\rangle \tag{2.45}$$
$$|4\rangle = -\sin\theta\,|+-\rangle + \cos\theta\,|-+\rangle \tag{2.46}$$

As the mixing angle depends on the static magnetic field, which reaches from 0 to infinity the mixing angle reaches from 0 (corresponding to infinity magnetic field) to $\frac{\pi}{4}$ (corresponding to zero magnetic field). In those limits the two states are

$$|2\rangle = |+-\rangle \qquad \theta = 0 \tag{2.47}$$

$$|4\rangle = |-+\rangle \qquad \theta = 0 \tag{2.48}$$

$$|2\rangle = \frac{1}{\sqrt{2}}(|+-\rangle + |-+\rangle) \qquad \theta = \frac{\pi}{4} \tag{2.49}$$

$$|4\rangle = \frac{1}{\sqrt{2}}(-|+-\rangle + |-+\rangle) \qquad \theta = \frac{\pi}{4} \tag{2.50}$$

At zero static magnetic field the final states are superpositions of the two base states which get uncoupled in high magnetic fields. At $B = 0$ the energy difference is $4A$, so the coefficient A is one fourth of the transition frequency ν_0 at zero magnetic field

$$A = \frac{h\nu_0}{4} \tag{2.51}$$

therefore the four energy levels are

$$E_1 = \frac{h\nu_0}{4} + \frac{1}{2}(g_J + g_I)\mu_\mathrm{B}B \tag{2.52}$$

$$E_2 = -\frac{h\nu_0}{4} + \frac{h\nu_0}{2}\sqrt{1 + \left(\frac{B}{B_\mathrm{C}}\right)^2} \tag{2.53}$$

$$E_3 = \frac{h\nu_0}{4} - \frac{1}{2}(g_J + g_I)\mu_\mathrm{B}B \tag{2.54}$$

$$E_4 = -\frac{h\nu_0}{4} - \frac{h\nu_0}{2}\sqrt{1 + \left(\frac{B}{B_\mathrm{C}}\right)^2} \tag{2.55}$$

The σ_1-transition is the transition between state $|2\rangle$ and state $|4\rangle$ and the π_1-transition is the transition between state $|1\rangle$ and state $|4\rangle$. The transition frequencies follow from eq. (2.52) - (2.55)

$$\nu_{\sigma_1} = \frac{E_2 - E_4}{h} = \nu_0\sqrt{1 + \left(\frac{(g_I - g_J)\mu_\mathrm{B}B}{\nu_0 h}\right)^2} \tag{2.56}$$

$$\nu_{\pi_1} = \frac{E_1 - E_4}{h} = \frac{\nu_0}{2} + \frac{(g_J + g_I)\mu_\mathrm{B}B}{2h} + \frac{\nu_0}{2}\sqrt{1 + \left(\frac{(g_I - g_J)\mu_\mathrm{B}B}{\nu_0 h}\right)^2} \tag{2.57}$$

The Breit Rabi diagram in fig. 2.1 shows the behaviour of the states in an external magnetic field. The triplet state splits, two of the states are increasing with the magnetic field - this is why they are called low-field-seekers (LFS) - and the other state and the singlet state are decreasing with increasing magnetic field - they are called high-field-seekers (HFS). The σ_1- and π_1-transition are also shown.

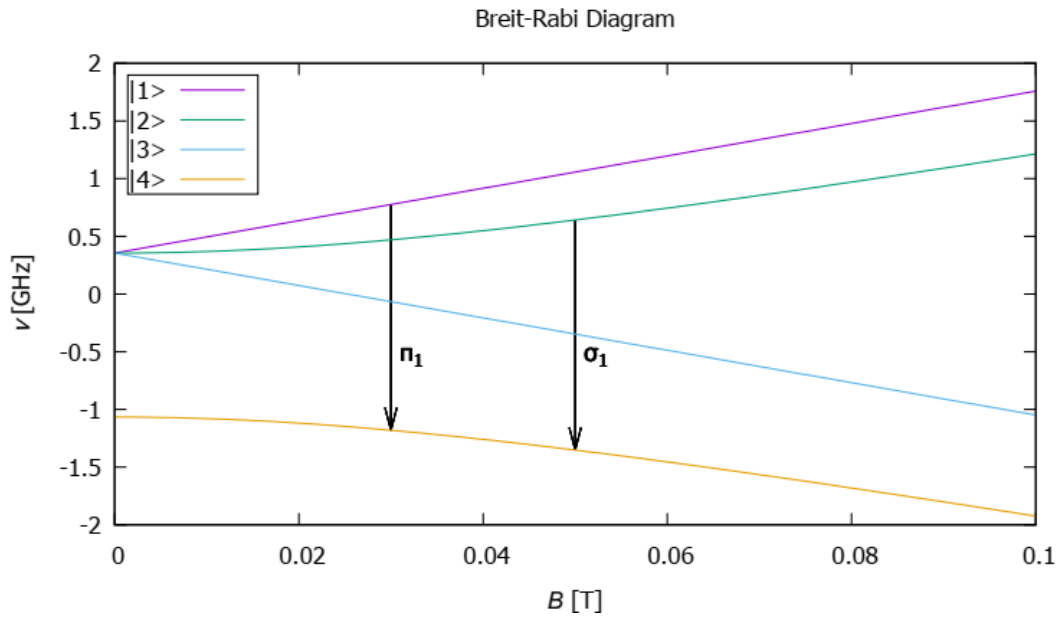

Figure 2.1: Hydrogen ground-state hyperfine splitting in external magnetic field. From [8].

External oscillating magnetic field

To induce the transitions an oscillating magnetic field can be applied. For the σ_1-transition the oscillating magnetic field and the static magnetic field have to be parallel. It can be seen easily by calculating the matrix elements that non-parallel components lead to vanishing matrix elements. Therefore the Hamiltonian gets

$$\hat{H}_\mathrm{I} = -(\mu_J \sigma_z^e + \mu_I \sigma_z^p) B_\mathrm{osc} \cos(\omega t) \tag{2.58}$$

For the σ_1 transition the matrix element $\langle 4| \hat{H}_\mathrm{I} |2\rangle$ has to be calculated.

$$\begin{aligned}
\langle 4| \hat{H}_\mathrm{I} |2\rangle &= (\langle +-| (-\sin\theta) + \langle -+| \cos\theta)(K_1 \sigma_z^e + K_2 \sigma_z^p)(\cos\theta |+-\rangle + \sin\theta |-+\rangle) \\
&= -\langle +-| \sin\theta K_1 \sigma_z^e \cos\theta |+-\rangle - \langle +-| sin^2\theta K_1 \sigma_z^e |-+\rangle \\
&\quad - \langle +-| \sin\theta K_2 \sigma_z^p \cos\theta |+-\rangle - \langle +-| sin^2\theta K_2 \sigma_z^p |-+\rangle \\
&\quad + \langle -+| cos^2\theta K_1 \sigma_z^e |+-\rangle + \langle -+| \sin\theta K_1 \sigma_z^e \cos\theta |-+\rangle \\
&\quad + \langle -+| cos^2\theta K_2 \sigma_z^p |+-\rangle + \langle -+| \cos\theta K_2 \sigma_z^p \sin\theta |-+\rangle
\end{aligned} \tag{2.59}$$

with $K_1 = -\mu_J B_\mathrm{osc} \cos(\omega t)$ and $K_2 = -\mu_I B_\mathrm{osc} \cos(\omega t)$. Using the Pauli matrices as shown in table 2.1 and with the fact that the states are orthogonal this leads to

$$\begin{aligned}
\langle 4| \hat{H}_\mathrm{I} |2\rangle &= -K_1 \cos\theta \sin\theta + K_2 \sin\theta \cos\theta - K_1 \cos\theta \sin\theta + K_2 \sin\theta \cos\theta \\
&= -2 \sin\theta \cos\theta B_\mathrm{osc} \cos(\omega t)(-\mu_J + \mu_I)
\end{aligned} \tag{2.60}$$

The matrix element $\langle i|\,\hat{H}_{\mathrm{I}}\,|j\rangle = \mu_{ij} B_{\mathrm{osc}} \cos(\omega t)$ can be calculated and the so-called Rabi frequency

$$\Omega_{ij} = \frac{\mu_{ij} B_{\mathrm{osc}}}{\hbar} \tag{2.61}$$

can be introduced. The Rabi frequency gives the oscillation frequency of two given atomic energy levels. The correlation between the matrix element and the Rabi frequency is given by

$$\Omega_{ij} \hbar \cos(\omega t) = \hat{H}_{ij} \tag{2.62}$$

The maximal state conversation probability is reached when the Rabi frequency is [8]

$$\Omega_{\mathrm{R}} = \frac{\pi}{t} \tag{2.63}$$

Plugging this into eq. 2.60, using $\mu_J = \frac{g_J \mu_{\mathrm{B}}}{2}$, $\mu_I = \frac{g_I \mu_{\mathrm{B}}}{2}$ and solving for the oscillating magnetic field yields

$$B_{\mathrm{osc},\sigma} = \frac{\pi \hbar}{t \sin\theta \cos\theta (g_I - g_J) \mu_{\mathrm{B}}} \tag{2.64}$$

For the π_1-transition the matrix element $\langle 4|\,\hat{H}_{\mathrm{I}}\,|1\rangle$ is relevant. The interaction Hamiltonian changes because for the π_1-transition the matrix elements vanish for parallel oscillating and static magnetic field. So without loss of generality setting the x-axis as the axis of the oscillating magnetic field the Hamiltonian is

$$\hat{H}_{\mathrm{I}} = K_1 \sigma_x^e + K_2 \sigma_x^p \tag{2.65}$$

which yields

$$\begin{aligned} \langle 4|\,\hat{H}_{\mathrm{I}}\,|1\rangle &= (\langle +-|\,(-\sin\theta) + \langle -+|\cos\theta)(K_1 \sigma_x^e K_2 \sigma_x^p)\,|++\rangle \\ &= \frac{(g_I \sin\theta - g_J \cos\theta)\mu_{\mathrm{B}} B_{\mathrm{osc}} \cos(\omega t)}{2} \end{aligned} \tag{2.66}$$

The same investigation done for the σ-transition can be done for the π-transition which leads to an oscillating magnetic field of

$$B_{\mathrm{osc},\pi_1} = \frac{2\pi\hbar}{t(g_I \sin\theta - g_J \cos\theta)\mu_{\mathrm{B}}} \tag{2.67}$$

The behaviour of the transition probability dependent on the mixing angle is shown is fig. 2.2.The σ-transition probability is 0 at an infinitely large static magnetic field because the state is not a superposition anymore and the transition can not happen. The region where the data were measured used in this thesis (indicated as the red area

in fig. 2.2) shows that the transition probability for the σ-transition stays the same while for the π-transition the change is about 0.4 %.

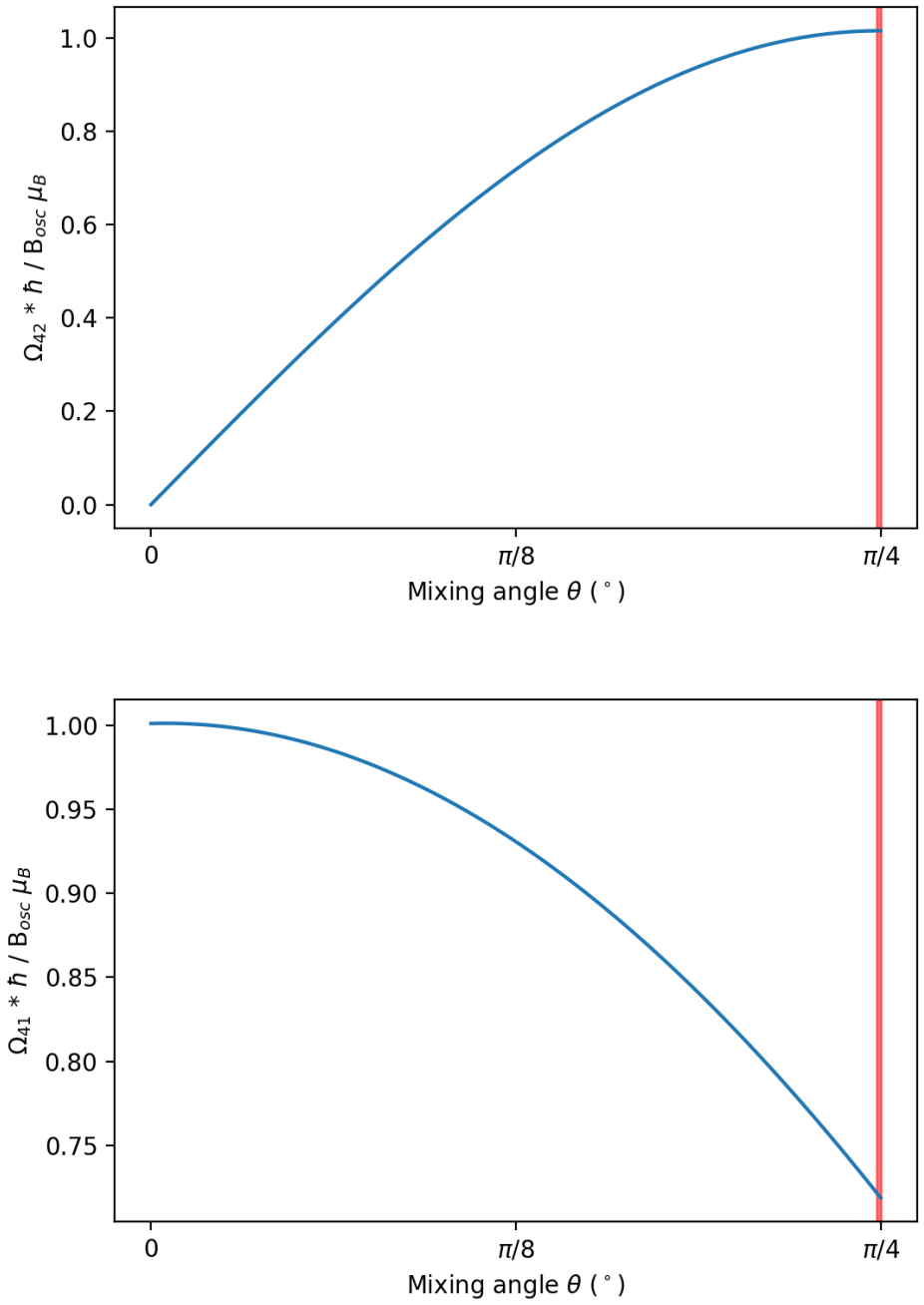

Figure 2.2: Top: Behaviour of the transition probability for the σ-transition in dependence on the mixing angle.
Bottom: Behaviour of the transition probability for the π-transition in dependence on the mixing angle.
The red area indicates the measured range in this thesis.

Fourlevel system

At a high static magnetic field the states are separated wide enough so that it is sufficient to include the initial and final state when deriving the experimental line profile, i.e. the system can be solved as a two-level system. In the low magnetic field region the transition frequencies get close to each other, so that all transitions have to be taken into account and a four-level system has to be solved which is described in this section.

The wavefunction of the system is given by

$$\Psi(\vec{x},t) = c_1(t)\Psi_1(\vec{x},t) + c_2(t)\Psi_2(\vec{x},t) + c_3(t)\Psi_3(\vec{x},t) + c_4(t)\Psi_4(\vec{x},t) \tag{2.68}$$

which is normalized at all time $\int d^3x |\Psi(\vec{x},t)|^2 = \sum_{i=1}^{4} |c_i(t)|^2 = 1$. Every wavefunction can be written as $\Psi_i(\vec{x},t) = \psi_i(\vec{x})e^{-\frac{iE_it}{\hbar}}$ and therefore solves the Schrödinger equation of the undisturbed Hamiltonian as $\hat{H}\Psi_i(\vec{x},t) = E_i\Psi(\vec{x},t)$.

Plugging equation (2.68) into the Schrödinger equation yields

$$\hat{H}_{\mathrm{I}}(c_1\Psi_1 + c_2\Psi_2 + c_3\Psi_3 + c_4\Psi_4) = i\hbar\left(\Psi_1\frac{dc_1}{dt} + \Psi_2\frac{dc_2}{dt} + \Psi_3\frac{dc_3}{dt} + \Psi_4\frac{dc_4}{dt}\right) \tag{2.69}$$

Multiplying this equation from the left by Ψ_i^* (with i = 1,...,4) and integrating over the whole space leads to four equations for the coefficients [19]

$$i\hbar\frac{dc_1}{dt} = \langle 1|\hat{H}_{\mathrm{I}}|1\rangle c_1 + e^{-i\omega_{12}t}\langle 1|\hat{H}_{\mathrm{I}}|2\rangle c_2 + e^{-i\omega_{13}t}\langle 1|\hat{H}_{\mathrm{I}}|3\rangle c_3 + e^{-i\omega_{14}t}\langle 1|\hat{H}_{\mathrm{I}}|4\rangle c_4 \tag{2.70}$$

$$i\hbar\frac{dc_2}{dt} = e^{-i\omega_{21}t}\langle 2|\hat{H}_{\mathrm{I}}|1\rangle c_1 + \langle 2|\hat{H}_{\mathrm{I}}|2\rangle c_2 + e^{-i\omega_{23}t}\langle 2|\hat{H}_{\mathrm{I}}|3\rangle c_3 + e^{-i\omega_{24}t}\langle 2|\hat{H}_{\mathrm{I}}|4\rangle c_4 \tag{2.71}$$

$$i\hbar\frac{dc_3}{dt} = e^{-i\omega_{31}t}\langle 3|\hat{H}_{\mathrm{I}}|1\rangle c_1 + e^{-i\omega_{32}t}\langle 3|\hat{H}_{\mathrm{I}}|2\rangle c_2 + \langle 3|\hat{H}_{\mathrm{I}}|3\rangle c_3 + e^{-i\omega_{34}t}\langle 3|\hat{H}_{\mathrm{I}}|4\rangle c_4 \tag{2.72}$$

$$i\hbar\frac{dc_4}{dt} = e^{-i\omega_{41}t}\langle 4|\hat{H}_{\mathrm{I}}|1\rangle c_1 + e^{-i\omega_{42}t}\langle 4|\hat{H}_{\mathrm{I}}|2\rangle c_2 + e^{-i\omega_{43}t}\langle 4|\hat{H}_{\mathrm{I}}|3\rangle c_3 + \langle 4|\hat{H}_{\mathrm{I}}|4\rangle c_4 \tag{2.73}$$

It is used that $\omega_{ij} = \frac{E_i - E_j}{\hbar}$, $\int d^3x\psi_i^*\hat{H}_{\mathrm{I}}\psi_j = \langle i|\hat{H}_{\mathrm{I}}|j\rangle$ and that ψ_i and ψ_j are orthogonal for $i \neq j$. The interaction Hamiltonian $\hat{H}_{\mathrm{I}} = \vec{\mu}\vec{B_{\mathrm{osc}}}\cos(\omega t)$ describes the interaction between the atom and an external oscillating magnetic field. The integrands $\psi^*\hat{H}_{\mathrm{I}}\psi$ are odd functions of position which leads to vanishing diagonal elements $\langle i|\hat{H}_{\mathrm{I}}|i\rangle = 0$ [19]. The off-diagonal elements do not vanish if the two transition states have opposite parity $\langle i|\hat{H}_{\mathrm{I}}|j\rangle = \mu_{ij}B_{\mathrm{osc}}\cos(\omega t)$ with μ_{ij} is the magnetic transition moment for the states i and j.

Using all these equations and the definition of the Rabi frequency in eq. (2.61), the four differential equations (2.70) - (2.73) become

$$i\frac{dc_1}{dt} = \left(e^{-i\omega_{12}t}\Omega_{12}c_2 + e^{-i\omega_{13}t}\Omega_{13}c_3 + e^{-i\omega_{14}t}\Omega_{14}c_4\right)\cos(\omega t) \tag{2.74}$$

$$i\frac{dc_2}{dt} = \left(e^{-i\omega_{21}t}\Omega_{21}c_1 + e^{-i\omega_{23}t}\Omega_{23}c_3 + e^{-i\omega_{24}t}\Omega_{24}c_4\right)\cos(\omega t) \tag{2.75}$$

$$i\frac{dc_3}{dt} = \left(e^{-i\omega_{31}t}\Omega_{31}c_1 + e^{-i\omega_{32}t}\Omega_{32}c_2 + e^{-i\omega_{34}t}\Omega_{34}c_4\right)\cos(\omega t) \tag{2.76}$$

$$i\frac{dc_4}{dt} = \left(e^{-i\omega_{41}t}\Omega_{41}c_1 + e^{-i\omega_{42}t}\Omega_{42}c_2 + e^{-i\omega_{43}t}\Omega_{43}c_3\right)\cos(\omega t) \tag{2.77}$$

Now everything is prepared to go further and use the density matrix formalism. In this formalism the von Neumann equation

$$\frac{d\hat{\rho}}{dt} = \frac{i}{\hbar}\left[\hat{\rho}, \hat{H}\right] \tag{2.78}$$

has to be solved, where $\hat{\rho} = |\psi\rangle\langle\psi|$ is the density matrix and $\hat{H}_{ij}$ is the Hamiltonian. In matrix form the density matrix can be expressed as

$$\hat{\rho} = \begin{pmatrix} c_1 \\ c_2 \\ c_3 \\ c_4 \end{pmatrix}\begin{pmatrix} c_1^*, & c_2^*, & c_3^*, & c_4^* \end{pmatrix} = \begin{pmatrix} |c_1|^2 & c_1c_2^* & c_1c_3^* & c_1c_4^* \\ c_2c_1^* & |c_2|^2 & c_2c_3^* & c_2c_4^* \\ c_3c_1^* & c_3c_2^* & |c_3|^2 & c_3c_4^* \\ c_4c_1^* & c_4c_2^* & c_4c_3^* & |c_4|^2 \end{pmatrix} \tag{2.79}$$

The density matrix represents the probability of finding the system in one state in the diagonal elements and coherences between states in the off-diagonal elements. Solving the von Neumann equation give a time evolution of the system under a certain interaction. Calculating $\frac{d\rho_{ij}}{dt} = c_i\frac{dc_j^*}{dt} + \frac{dc_i}{dt}c_j^*$ leads to ten independent equations, the so-called optical Bloch equations for the four-level system. As an example $\frac{d\rho_{11}}{dt}$ is calculated.

$$\begin{aligned}\frac{d\rho_{11}}{dt} =& i\big(\rho_{12}\Omega_{12}^*e^{i\omega_{12}t} + \rho_{13}\Omega_{13}^*e^{i\omega_{13}t} + \rho_{14}\Omega_{14}^*e^{i\omega_{14}t} \\ & - \rho_{21}\Omega_{12}e^{i\omega_{21}t} - \rho_{31}\Omega_{13}e^{i\omega_{31}t} - \rho_{41}\Omega_{14}e^{i\omega_{41}t}\big)\cos(\omega t)\end{aligned} \tag{2.80}$$

The Rabi frequency depends on the matrix element $\langle i|\,\mu\,|j\rangle$ so $\Omega_{ij} = \Omega_{ji}^*$ which are in general complex but real for transitions between bound states [19]. Using the substitutions $\rho'_{ij} = e^{i\omega_{ij}t}\rho_{ij}$ and $\rho'_{ii} = \rho_{ii}$ yields

$$\frac{d\rho'_{11}}{dt} = i\big(\Omega_{12}(\rho'_{12} - \rho'_{21}) + \Omega_{13}(\rho'_{13} - \rho'_{31}) + \Omega_{14}(\rho'_{14} - \rho'_{41})\big)\cos(\omega t) \tag{2.81}$$

The same procedure can be done with the other nine equations which gives

$$
\begin{aligned}
\frac{d\rho'_{22}}{dt} &= i\big(\Omega_{21}(\rho'_{21}-\rho'_{12})+\Omega_{23}(\rho'_{23}-\rho'_{32})+\Omega_{24}(\rho'_{24}-\rho'_{42})\big)\cos(\omega t)\\
\frac{d\rho'_{33}}{dt} &= i\big(\Omega_{31}(\rho'_{31}-\rho'_{13})+\Omega_{32}(\rho'_{32}-\rho'_{23})+\Omega_{34}(\rho'_{34}-\rho'_{32})\big)\cos(\omega t)\\
\frac{d\rho'_{44}}{dt} &= i\big(\Omega_{41}(\rho'_{41}-\rho'_{14})+\Omega_{42}(\rho'_{42}-\rho'_{24})+\Omega_{43}(\rho'_{43}-\rho'_{34})\big)\cos(\omega t)\\
\frac{d\rho'_{12}}{dt} &= i\big(\Omega_{12}(\rho'_{11}-\rho'_{22})+\rho'_{13}\Omega_{32}+\rho'_{14}\Omega_{42}-\rho'_{32}\Omega_{13}-\rho'_{42}\Omega_{14}\big)\cos(\omega t)+i\omega_{12}\rho'_{12}\\
\frac{d\rho'_{13}}{dt} &= i\big(\Omega_{13}(\rho'_{11}-\rho'_{33})+\rho'_{12}\Omega_{23}+\rho'_{14}\Omega_{43}-\rho'_{23}\Omega_{12}-\rho'_{43}\Omega_{14}\big)\cos(\omega t)+i\omega_{13}\rho'_{13}\\
\frac{d\rho'_{14}}{dt} &= i\big(\Omega_{14}(\rho'_{11}-\rho'_{44})+\rho'_{12}\Omega_{24}+\rho'_{13}\Omega_{34}-\rho'_{24}\Omega_{12}-\rho'_{34}\Omega_{13}\big)\cos(\omega t)+i\omega_{14}\rho'_{14}\\
\frac{d\rho'_{23}}{dt} &= i\big(\Omega_{23}(\rho'_{22}-\rho'_{33})+\rho'_{21}\Omega_{13}+\rho'_{24}\Omega_{43}-\rho'_{13}\Omega_{21}-\rho'_{43}\Omega_{24}\big)\cos(\omega t)+i\omega_{23}\rho'_{23}\\
\frac{d\rho'_{24}}{dt} &= i\big(\Omega_{24}(\rho'_{22}-\rho'_{44})+\rho'_{21}\Omega_{14}+\rho'_{23}\Omega_{34}-\rho'_{14}\Omega_{21}-\rho'_{34}\Omega_{23}\big)\cos(\omega t)+i\omega_{24}\rho'_{24}\\
\frac{d\rho'_{34}}{dt} &= i\big(\Omega_{34}(\rho'_{33}-\rho'_{44})+\rho'_{31}\Omega_{14}+\rho'_{32}\Omega_{24}-\rho'_{14}\Omega_{31}-\rho'_{24}\Omega_{32}\big)\cos(\omega t)+i\omega_{34}\rho'_{34}
\end{aligned}
\tag{2.82}
$$

These ten equations can be solved numerically for example with the Heun method (see chapter 5).

2.3 Standard Model Extension

As explained in chapter 2.1, CPT has to be invariant in the SM and to date there is also no contradicting experimental evidence. However there are models which do not need CPT invariance, for example the group of Kostelecký et al. proposed a Standard Model Extension (SME) in which Lorentz-invariance and CPT are broken [7]. This was done by adding all possible Lorentz-violating terms to the SM Lagrangian. Kostelecký et al. proposed various experiments to test their framework including the measurement of the hyperfine structure of hydrogen and antihydrogen [20].

For the hydrogen respectively antihydrogen energy spectrum the relevant Lorentz-violating term arises from corrections to the propagation of the electron or proton. Therefore the Lagrange density of interest is given by

$$
\mathcal{L} \subset \frac{1}{2}\overline{\psi}_\omega(\gamma^\mu i\partial_\mu - m_\omega + \mathcal{Q}_\omega)\psi_\omega + \text{h.c.} \tag{2.83}
$$

where ω is a flavour index indicating the electron or the proton, ψ_ω is a quantum fermion field with mass m_ω and $\mathcal{Q}_\omega$ is a spinor matrix calculated from the sum of all terms formed by contracting SME coefficients for the Lorentz- and CPT violation with terms $i\partial_\mu$ [20].

Deriving the energy shifts due to these Lorentz- and CPT violating terms would go

beyond the scope of this thesis. The Lorentz- and CPT-violating terms lead to a shift of the hyperfine splitting at zero magnetic field which results in a cancellation of degeneration of the energy triplet. The difference between the hydrogen and antihydrogen hyperfine frequency of a transition of $\Delta m_F = 1$ is calculated to

$$2\pi\Delta\nu = -\frac{1}{\sqrt{3\pi}}\sum_{q=0}^{2}(\alpha m_r)^{2q}(1+4\delta_{q2})\cdot\sum_{\omega}(g^{\mathrm{NR}(0B)}_{\omega_{(2q)10}} + 2g^{\mathrm{NR}(1B)}_{\omega_{(2q)10}}) \tag{2.84}$$

with $\delta_{(2q)}$ is the Kronecker Delta, α the fine structure constant, m_r the reduced mass and $g^{\mathrm{NR}(0B)}_{\omega_{(2q)10}}$ respectively $g^{\mathrm{NR}(1B)}_{\omega_{(2q)10}}$ are the coefficients of interest, where the superscript NR denotes non-relativistic and $(0B)$ respectively $(1B)$ indicate two terms of odd parity.

The possible Lorentz- and CPT-violation of the proton was tested by searching sidereal variations of the $F = 1$, $\Delta m_F = \pm 1$ Zeeman-splitting of hydrogen using a hydrogen maser, resulting in setting a boundary of 10^{-27} GeV [21]. Fig. 2.3 shows the effect of the SME on the energy levels of antihydrogen.

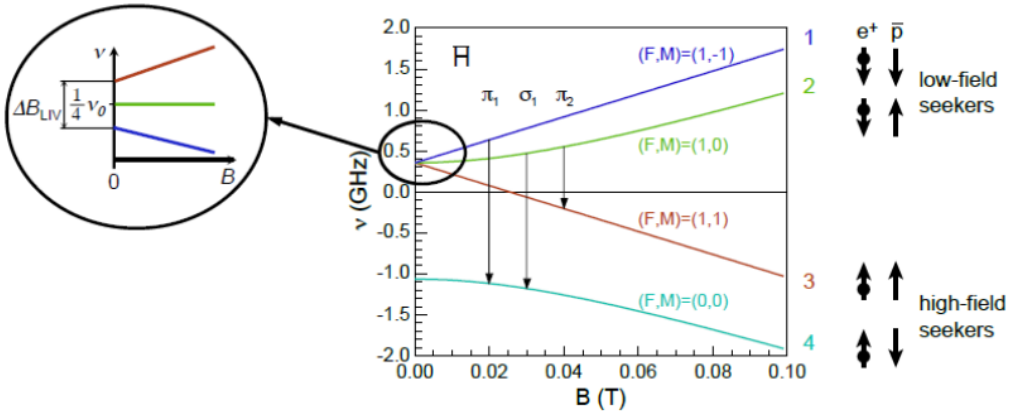

Figure 2.3: Antihydrogen ground-state hyperfine splitting for CPT symmetry violation. From [8].

Chapter 3

Experimental setup

In this section the experimental method is described. It is in principle a Rabi experiment which is explained in the first part of the chapter while the second part deals with the hydrogen beam experimental setup specifically.

3.1 Rabi Experiment

To measure the magnetic moment of nuclei I. I. Rabi invented a new technique in 1939 [22]. As anomalies of the magnetic moment would be rather small the precision of the measurement was of significance. A schematic view of the method is shown in fig. 3.1.

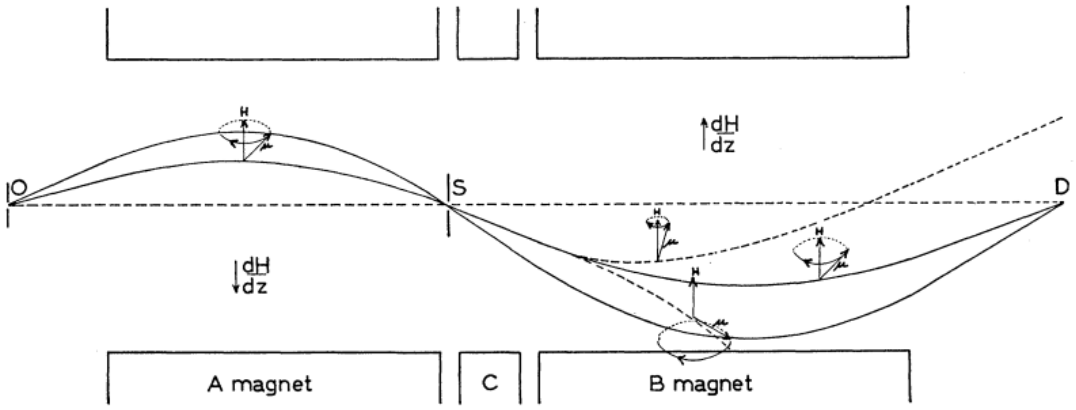

Figure 3.1: Schematic view of the path of molecules. The continuous lines are the paths of two molecules having different momenta, the dashed lines are the paths of two molecules which magnetic moments have changed because of an oscillating magnetic field applied in the region of magnet C inducing spin flips. From [22].

A beam coming from the source O traverses the inhomogeneous magnetic field produced by magnet A. The beam gets polarized according to the orientation of the magnetic moments. Atoms with the proper momentum get collimated through the slit S

followed by a static magnetic field produced by magnet C. Magnet B produces an inhomogeneous magnetic field having the same strength as magnet A but a field gradient in opposite direction. This leads to a deflection of the atoms as strong as the deflection in magnet A but in opposite direction, so the atoms hit the detector.

In an external magnetic field the magnetic moment $\vec{\mu} = \gamma \vec{J}$, where γ is the gyromagnetic ratio, precesses around the direction of the magnetic field with the so-called Larmor-frequency $\omega_L = g_J \frac{q}{2m} B$. The orientation of the magnetic moment is quantized. A transition between those orientations can be triggered by an oscillating magnetic field which oscillates with the Larmor-frequency. This oscillating field is applied at magnet C perpendicular to the static magnetic field. Having a change in the direction of the magnetic moment - generating a spinflip - leads to a different deflection of the atoms in magnet B which result in a drop of intensity in the detector.

3.2 Hydrogen beam experiment

This spectroscopy method can also be used for measuring the ground-state hyperfine structure of hydrogen/antihydrogen. For this purpose the hydrogen beam apparatus was built. The two LFS states of the hydrogen are focused by the polarizing magnets while the two HFS states are getting deflected. After applying a frequency close to the transition frequency some of the LFS states will flip to a HFS state and will be deflected by the analysing magnets resulting in a reduction of intensity in the detector. In fig. 3.2 and 3.3 a photograph and a schematic view of the hydrogen beam experiment are shown, respectively. This section gives a brief overview of the experiment, further details can be found in [23].

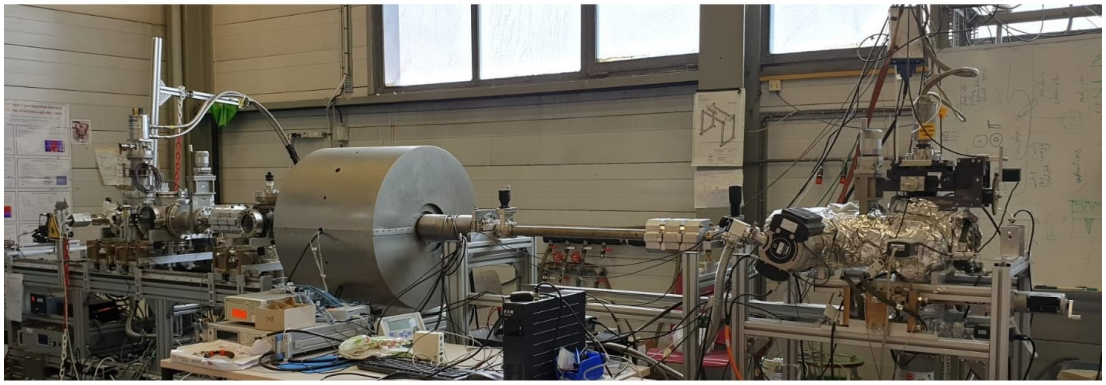

Figure 3.2: Picture of the hydrogen beam experiment.

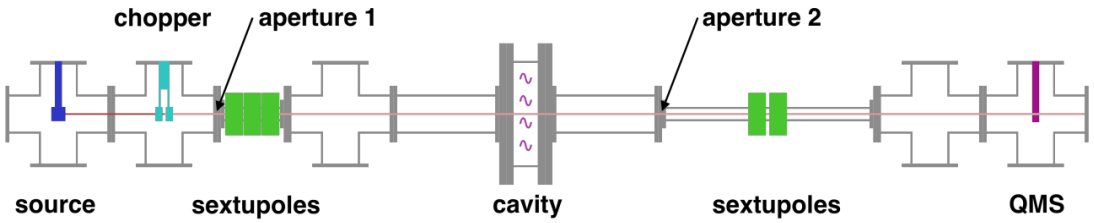

Figure 3.3: Schematic view of the hydrogen beam experiment with orthogonal hydrogen injection. The hydrogen atoms produced in the source pass the chopper which modulates the beam. The apertures select atoms following trajectories with certain radii. The first sextupole magnets polarize the beam followed by the cavity which induces the transition. The second sextupole magnets deflect the atoms which transitioned into a different state which result in a drop in the count rate at the QMS. From [9]

3.2.1 Hydrogen source

For this measurement ultra pure molecular hydrogen is produced by a Packard 9100 hydrogen generator by electrolysis of deionised water. The H_2 has to be dissociated to get atomic hydrogen which happens in a pyrex glass tube shown in fig. 3.4.

The molecular hydrogen enters the glass tube from the left. The tube is surrounded by a microwave antenna which radiates into its volume. The microwave antenna is fed by two N-type coaxial cables. Igniting the plasma (pink in left picture of fig. 3.5) with a spark gun leads to the production of atomic hydrogen which leaves the source on the right side of fig. 3.4.

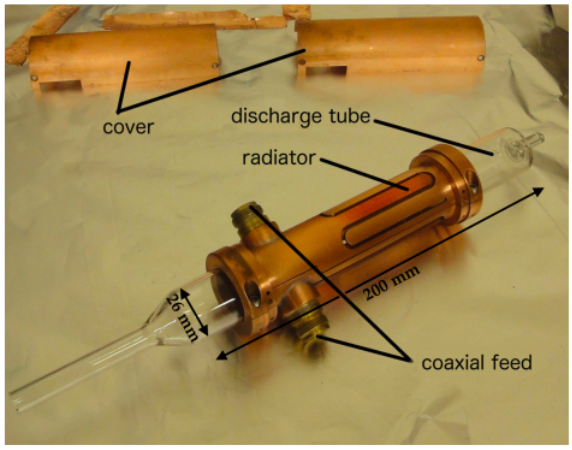

Figure 3.4: Hydrogen source to produce atomic hydrogen. From [23].

The atomic hydrogen is then led to a cooling system (fig. 3.5) either perpendicular or parallel to the beamline. In the parallel configuration more hydrogen at higher velocities can pass as they are interacting less with the surrounding while the perpendicular configuration forces more atoms to cool down via interaction with the wall, but this also

results in increased recombination. The atoms get decelerated by interaction with PTFE tubing sandwiched between the aluminium blocks which are cooled by a cryocooler (right picture of 3.5).

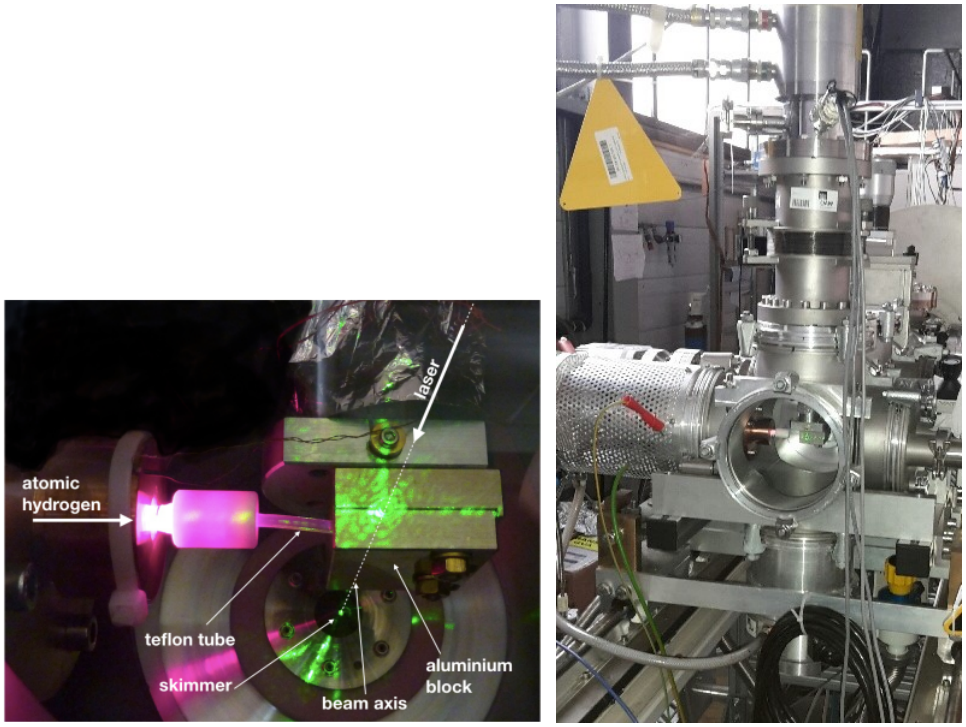

Figure 3.5: Left: Picture of the hydrogen injection into the vacuum chamber with the cooler. The green laser is for alignment and shows the beamaxis. From [23]. Right: Picture of the coldhead and perpendicular hydrogen injection.

3.2.2 Chopper, lock in amplifier, magnets & apertures

After the atoms are cooled the beam is modulated by a tuning fork chopper (Scitec CH-10, fig. 3.6) driven at a frequency of about 178 Hz with a duty cycle of 50 %. That gives on the one hand a background suppression and on the other hand a time of flight measurement. The background suppression is achieved by a lock in amplifier (LIA). It can extract the periodic signal induced by the tuning fork chopper of known frequency [24]. One period of the chopper is divided into 200 bins each representing one phase bin. In each bin the signal gets accumulated during a given time, which is longer than the chopper period, such that the LIA has enough signal to work with. At the end a histogram of counts per bin can be produced from which one can extract background, amplitude and phase shift (see section 4).

To polarise the beam and analyse it after the cavity permanent magnets are used. The magnets are in a Halbach-configuration (fig. 3.7) generating the desired magnetic

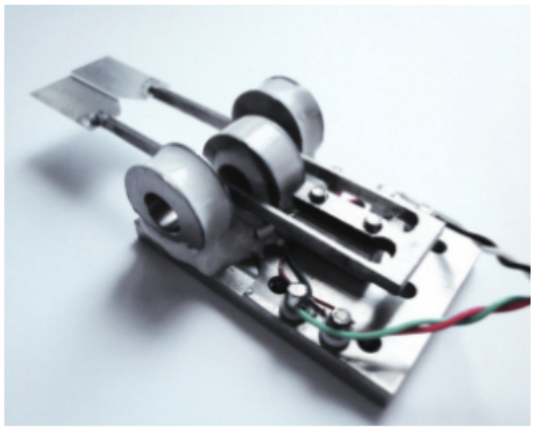

Figure 3.6: Picture of the tuning fork chopper. From [24].

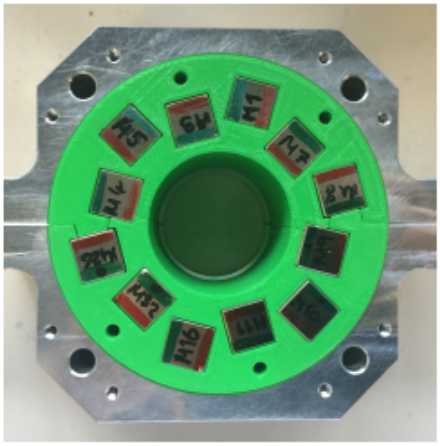

Figure 3.7: Permanent magnets for polarising and analysing. From [9].

field gradient. The 12 magnets with dimension 50 mm x 15 mm x 15 mm are made of NdFeB and are twisted 120 ° to each other.

From fig. 3.8 it can be seen that the states $|1\rangle$ and $|2\rangle$ follow different trajectories which leads to different intensities at the detector. This is because of the opposite force of the the two states in a magnetic field gradient. Ring apertures are used after the chopper and the cavity (fig. 3.9). These apertures block the central component of the hydrogen beam and allow only atoms at a certain radius between 12 and 18 mm to pass.

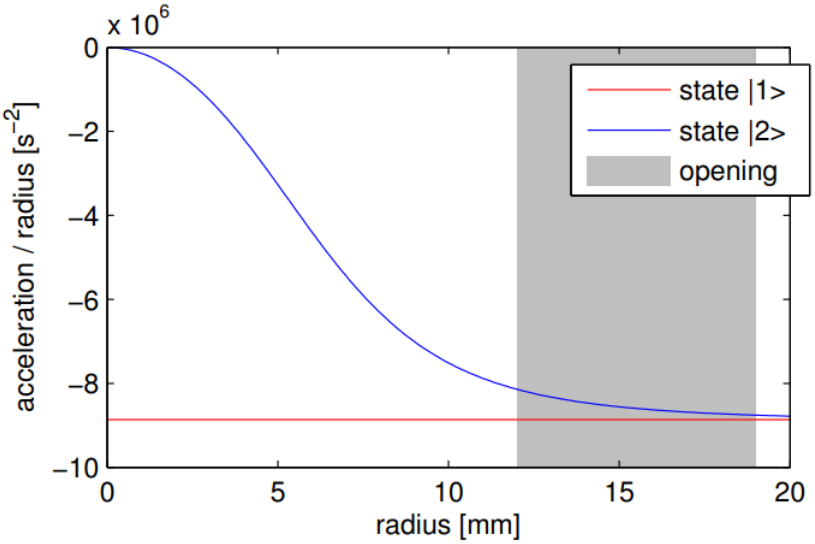

Figure 3.8: Simulation of the relative acceleration in radial direction for the hydrogen states $|1\rangle$ and $|2\rangle$ in a magnetic field with a field strength of $1600\,\mathrm{Tm}^{-2}$. The grey area indicates the opening of the apertures. From [9].

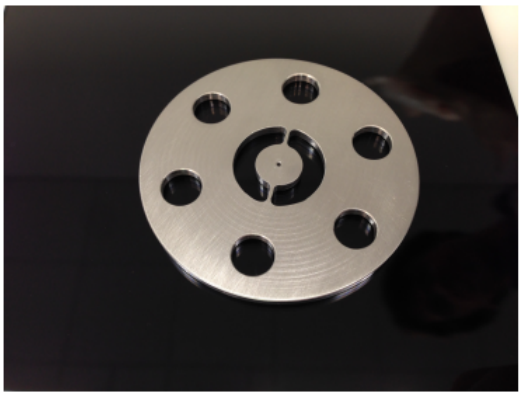

Figure 3.9: Ring aperture used to select a trajectory of a radius between 12 and 18 mm. The small hole in the center is for the Laser to pass for alignment. From [8].

3.2.3 Cavity

The central part of the experiment is the spin-flip cavity to induce the transition from a LFS to a HFS. This cavity was designed and built in 2012 [25]. The magnetic field is oscillating parallel to the long edge of the strip lines and has to be homogeneous in the x-y-plane at least along the beampipe. Because of these requirements a strip line geometry was chosen. In fig. 3.10 a picture of the cavity is shown, in fig. 3.11 the magnetic field inside the cavity is depicted.

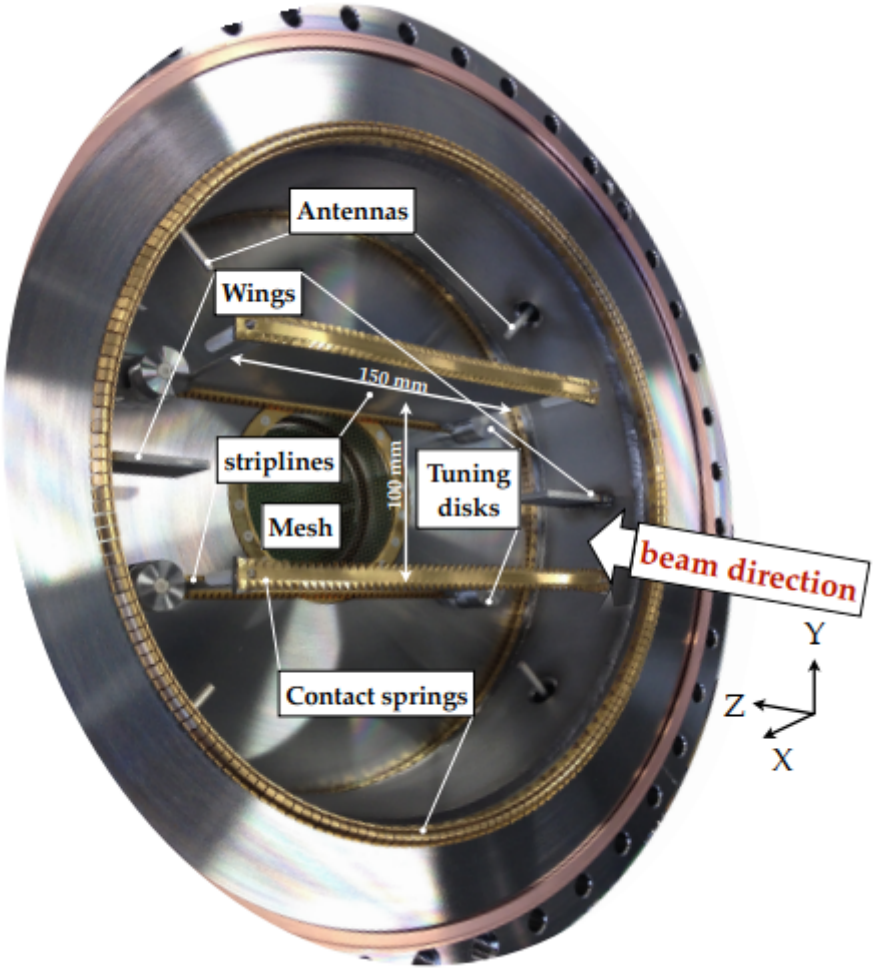

Figure 3.10: Photograph of the cavity. From [23].

As a strip line geometry has two different modes at nearly the same frequency additional wings were mounted to detune the unwanted one. To avoid a leakage of microwaves out of the cavity a mesh was installed at the entrance and exit. The antennas are used for coupling the microwaves into the cavity and as a pick-up of the signal to analyse it with a vector network analyser.

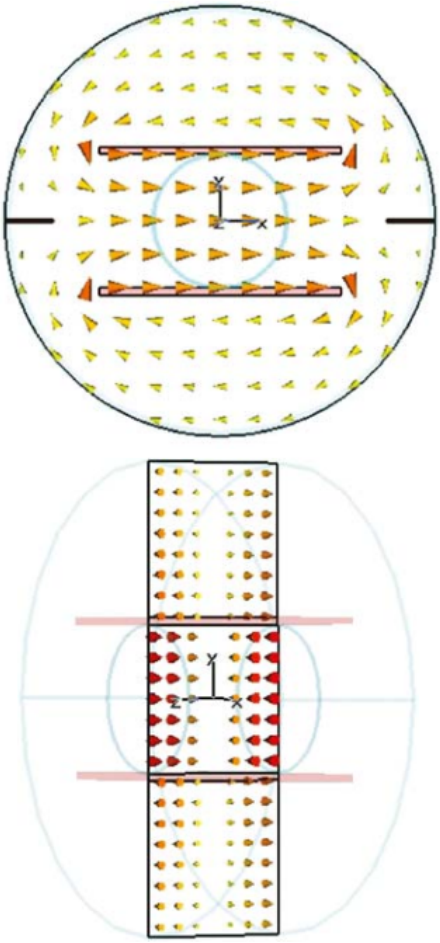

Figure 3.11: Top: Oscillating magnetic field of the cavity in x-y-plane. Bottom: Oscillating magnetic field inside the cavity in y-z-plane. The beam direction is the z-axis. Both from [26].

For control of the Zeeman splitting a static external magnetic field is applied using normal conducting coils. As the π-transition is very sensitive to the magnetic field it has to be very homogeneous. Therefore a McKeehan-like configuration is used [27]. Fig. 3.12 shows a simulation of the produced homogeneous static magnetic field.

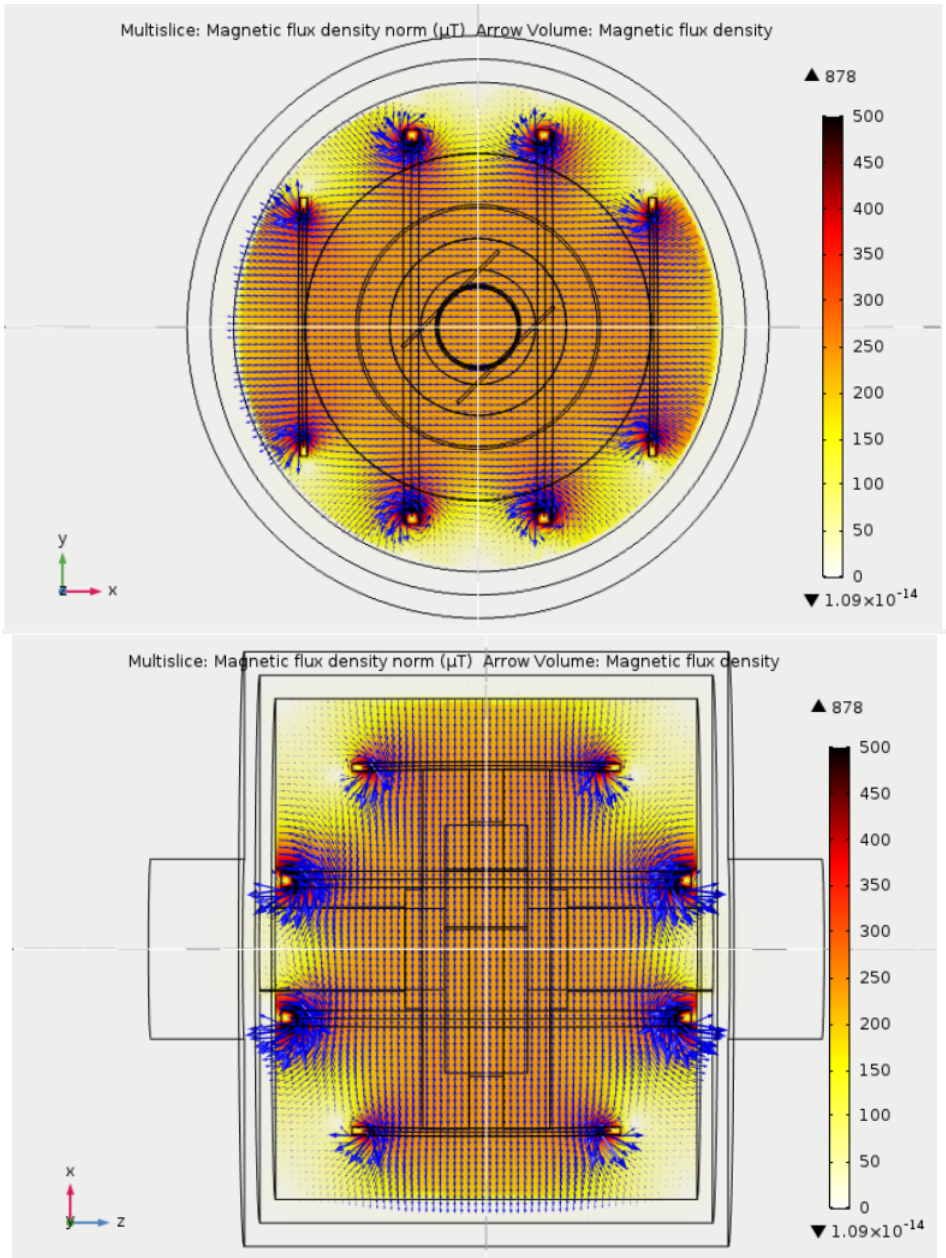

Figure 3.12: Top: Static magnetic field of the McKeehan coils in the x-y-plane. Bottom: Static magnetic field of the McKeehan coils in the x-z-plane. Both from [8].

3.2.4 Detector

The detector is a quadrupole mass spectrometer (QMS, fig. 3.13). The atoms enter a hole which is 3 mm in diameter and get ionized by interaction with electrons coming from a filament. After the ionization the ionized hydrogen atoms - now simply protons - enter four parallel rods on which constant and alternating electrical potentials are applied. The polarisation is in the same direction for each facing rods. Through the adjustment of the desired mass to charge ratio, only protons can pass the mass filter and are counted by a channeltron.

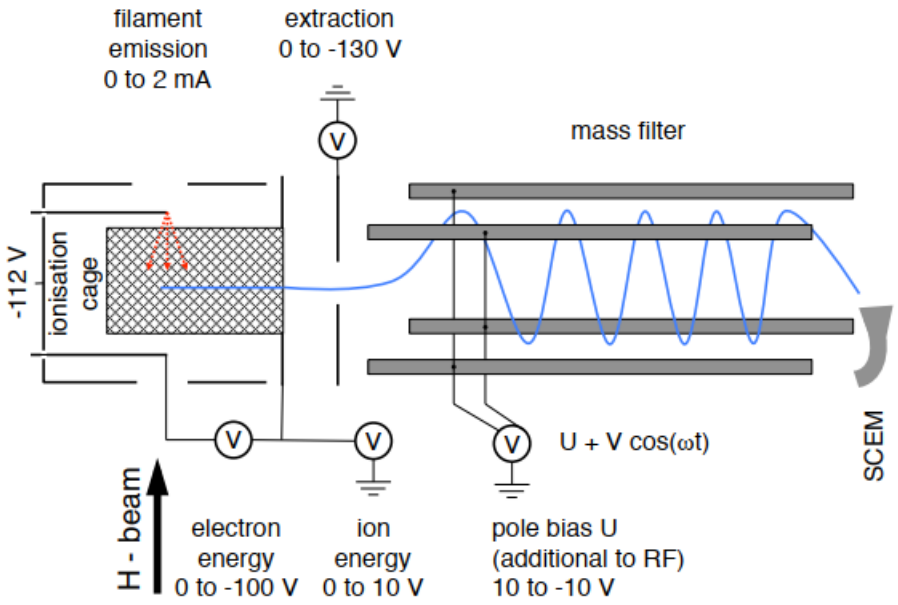

Figure 3.13: Sketch of the principle of the QMS. From [10].

Chapter 4

Analysis

The evaluation procedure, followed in this thesis with ROOT, is shown in fig. 4.1. The analysed data were taken in four measurement series in February and October 2017. The difference between these series is the magnitude of the static magnetic field in the cavity, while the apparatus itself and all other conditions were identical. In February the measurement was done in a higher magnetic field than in October, which leads to a wider Zeeman-shift. The coil currents and respective magnetic fields of the different measurements are listed in table 4.1.

Table 4.1: Different currents respectively magnetic field values of the measurement series. "X" indicates that this current was measured, "-" indicates that it was not measured.

Name	0.02 A (0.046 G)	0.06 A (0.139 G)	0.1 A (0.231 G)	0.3 A (0.694 G)	0.5 A (1.167 G)	1.9 A (4.398 G)
October Short Term (ST)	X	X	X	–	–	–
October Long Term (LT)	X	X	X	–	–	X
February	–	–	X	X	X	–

The October Short Term (ST) data consist of four sets measured from the fourth of October to the sixth of October. The October Long Term (LT) data consist of six sets taken from the ninth to the thirteenth of October and further six sets were taken from the sixteenth to the twentieth of October. The October LT data are split for the evaluation into two series because in the first half some problems with the data acquisition occurred. The terminology of the data acquisition used here is: Measuring one resonance curve, which means 41 histograms, is called a scan, 2 scans at the same magnetic field value is called a cycle and measuring 12 cycles in February respectively 16 cycles in October is called a set. From each set one value for the transition frequency can be evaluated. All together there are 43 sets to be evaluated.

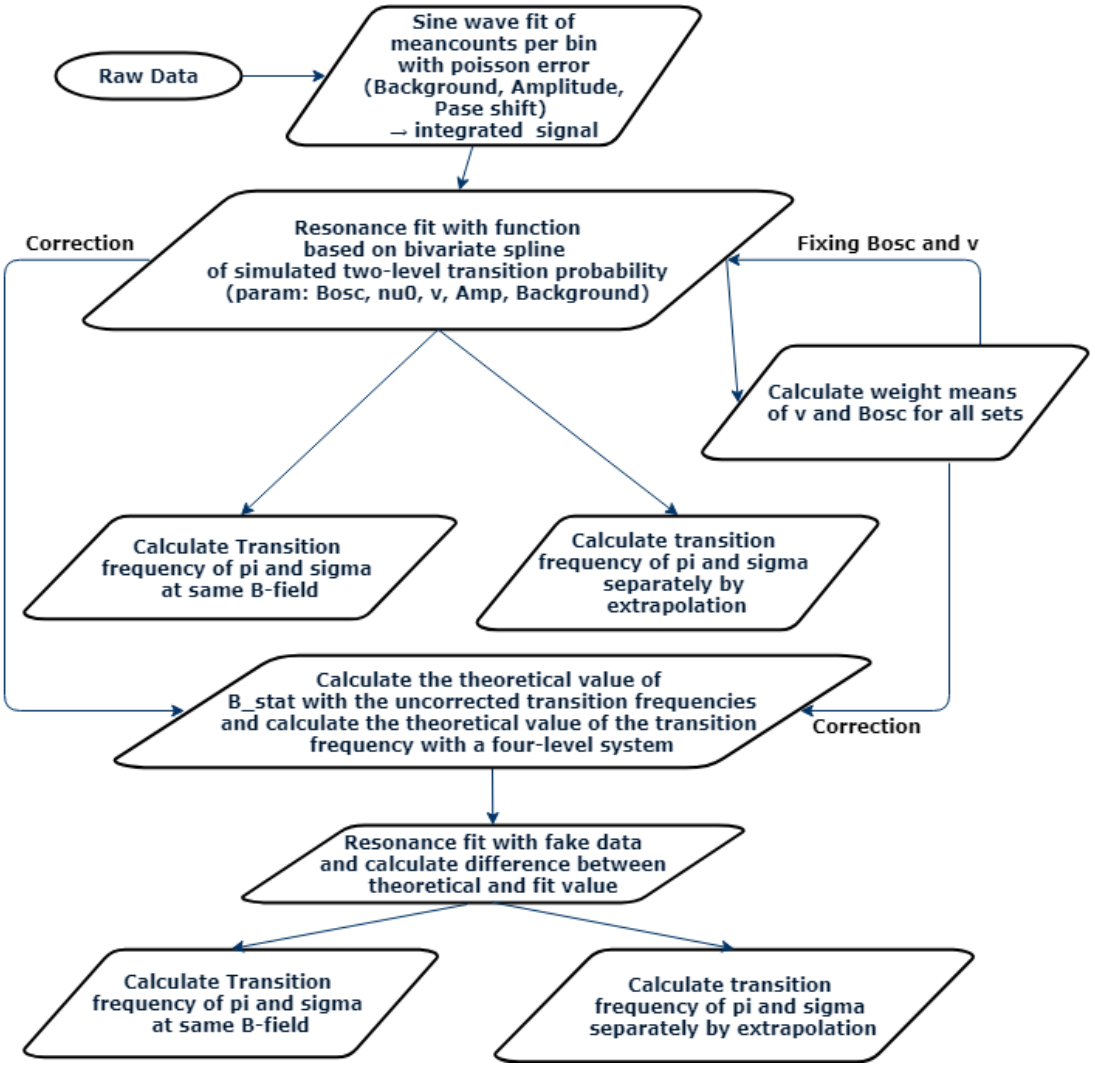

Figure 4.1: Schematic overview of the data evaluation and the systematic correction.

4.1 Raw signal

The experiment detects single particle events. This yields an accumulation of counts which can be plotted in a histogram using a Poisson error. The modulated signal is fitted with the positive half wave of a sine generated by the chopper

$$b + \frac{1}{2} A \left[\sin((x+\phi)2\pi) + \mid \sin((x+\phi)2\pi) \mid \right] \tag{4.1}$$

with b the baseline, A the amplitude, x the bin and ϕ the phase-shift. In fig. 4.2 an example for a sine-wave fit is shown.

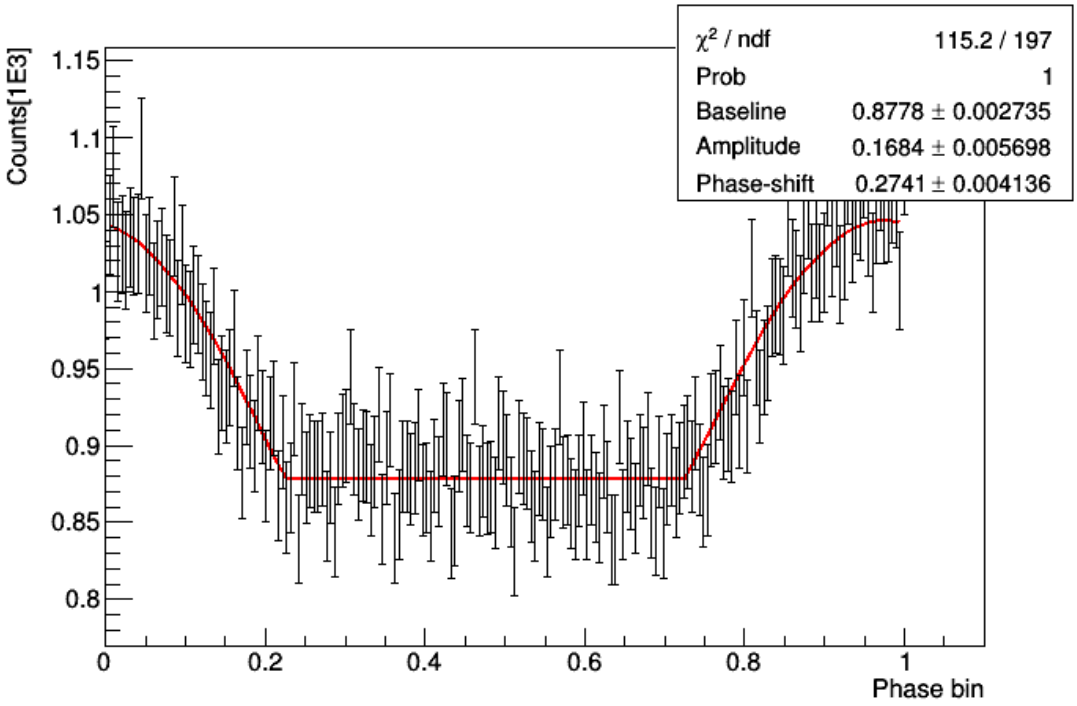

Figure 4.2: Histogram of counts per phase bin with a positive half wave of a sine as fit function (red). The errors used are poisson errors.

The signal, which is the sum of all counts above the baseline, can be extracted from this fit which is needed for the next step.

4.2 Resonance Fit

The experiment scans over a given frequency range symmetric around the so-called central frequency ν_0, which is the transition frequency at a given static magnetic field. Because of the geometry of the spin-flip cavity to produce a standing wave, a double-peak line shape arises from the zero-field crossing of the magnetic field along the beam propagation direction (fig. 4.3). There is no explicit analytical function for this line shape yet, hence the fit is done by a bivariate spline [9,10,28]. The transition probability depends on the oscillating magnetic field amplitude and the frequency detune $\Delta = \nu - \nu_0$, where ν is the microwave frequency. The transition probability was simulated for the σ_1-transition at discrete frequency and oscillating magnetic field points by C. Sauerzopf [29]. Using the simulated data the spline leads to a transition probability

$$\rho = \rho(\nu; v, B_{\text{osc}}, \Delta) \tag{4.2}$$

where the parameters are the beam velocity v, the oscillating magnetic field amplitude B_{osc} and the frequency detune Δ. The transition probability depends on the velocity distribution σ_v too but in this thesis it is set to 0 because of the narrow velocity

selection by the apertures. Fig. 4.4 shows the effect of changes in the parameters. The full resonance fit is then given by scaling the spline with the count rate drop at the detector A and the baseline b

$$Fit = -A\rho(\nu; v, B_{\text{osc}}, \Delta) + b \tag{4.3}$$

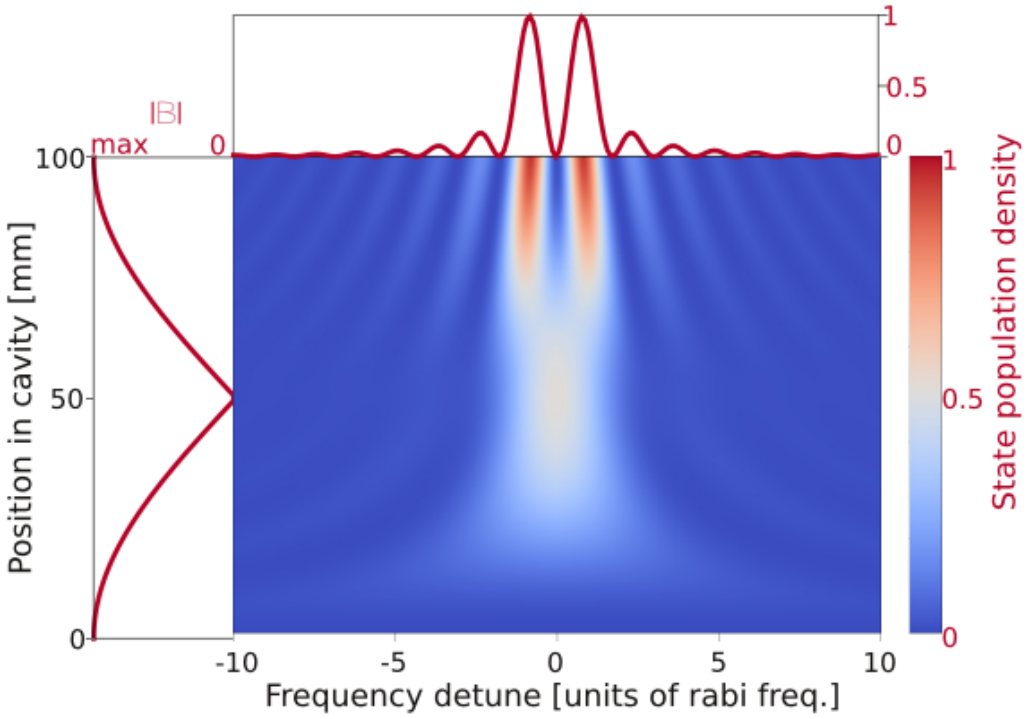

Figure 4.3: Center: Simulation of the state population dependent on the oscillating magnetic field amplitude and a frequency detune.
On the left: Distribution of the microwave amplitude along the cavity length and resulting state population density for different detuner.
On top: Double-peak line shape of the resonance curve.
From [29].

For each cycle 41 frequency steps are measured and analysed with the method described in 4.1. These signals are then fitted with the bivariate spline. For the February data, which were taken at rather high static magnetic field and already analysed in 2017 with Matlab, the Zeeman splitting is large enough for the treatment as effective two-level system. Going to lower magnetic fields, this assumption is not justified anymore (see section 5).

An example of the fitted resonance is shown in fig. 4.5. The free parameters are the oscillating magnetic field B_{osc}, the central frequency ν_0, i.e. the transition probability

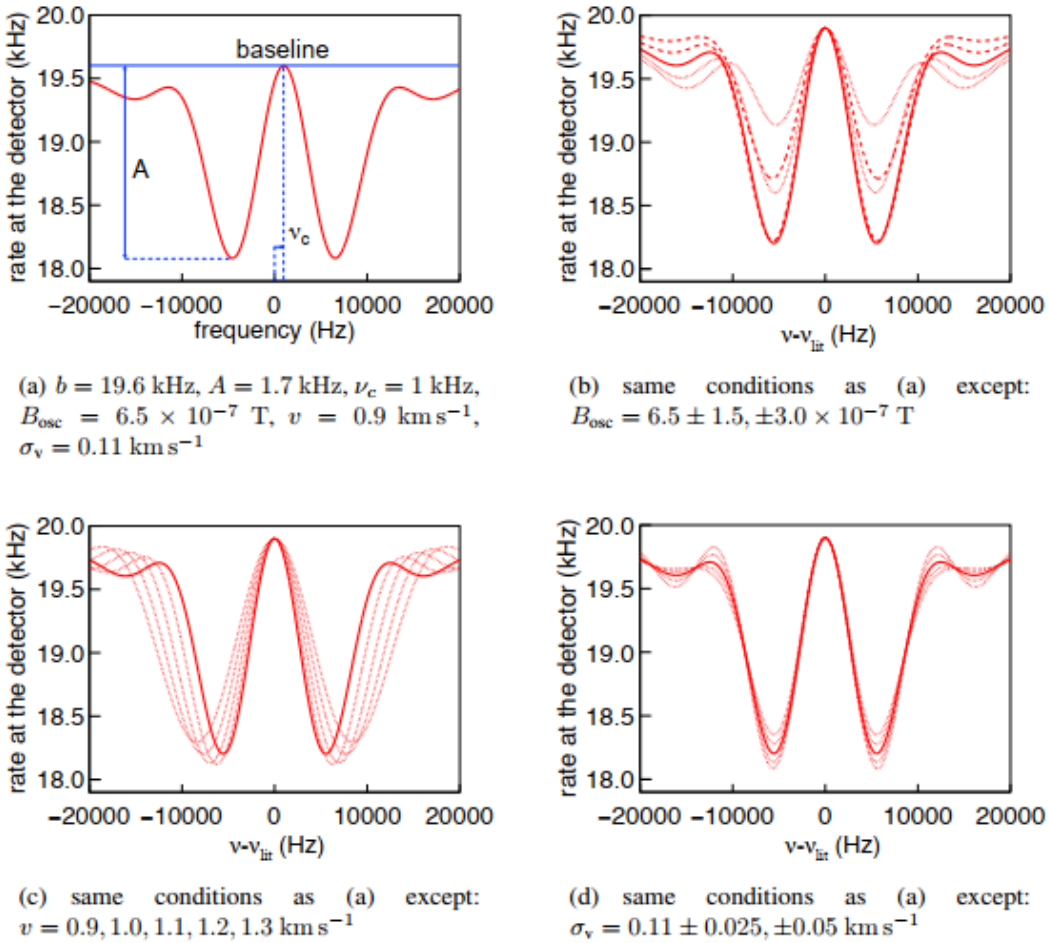

(a) $b = 19.6$ kHz, $A = 1.7$ kHz, $\nu_c = 1$ kHz, $B_{osc} = 6.5 \times 10^{-7}$ T, $v = 0.9$ km s^{-1}, $\sigma_v = 0.11$ km s^{-1}

(b) same conditions as (a) except: $B_{osc} = 6.5 \pm 1.5, \pm 3.0 \times 10^{-7}$ T

(c) same conditions as (a) except: $v = 0.9, 1.0, 1.1, 1.2, 1.3$ km s^{-1}

(d) same conditions as (a) except: $\sigma_v = 0.11 \pm 0.025, \pm 0.05$ km s^{-1}

Figure 4.4: Impact of the parameters of the resonance fit
(a): Resonance fit at a given central frequency, velocity and oscillating magnetic field value.
(b): Resonance fit with changed oscillating magnetic field amplitude.
(c): Resonance fit with changed beam velocity.
(d): Resonance fit with changed velocity distribution. From [10].

for a given magnetic field value, the beam velocity v, the amplitude A and the baseline b.

As the velocity and the oscillating magnetic field should not change in time, these parameters and the effect on the fit result of the central frequency are investigated further.

4.2.1 Analysis of beam velocity and oscillating magnetic field

Velocity

At first the beam velocity of each set is analysed. It defines the interaction time in the cavity and in consequence the shape of the resonance fit. As mentioned in subsection 3.2.2 the velocity for the two states is different and therefore the interaction time is

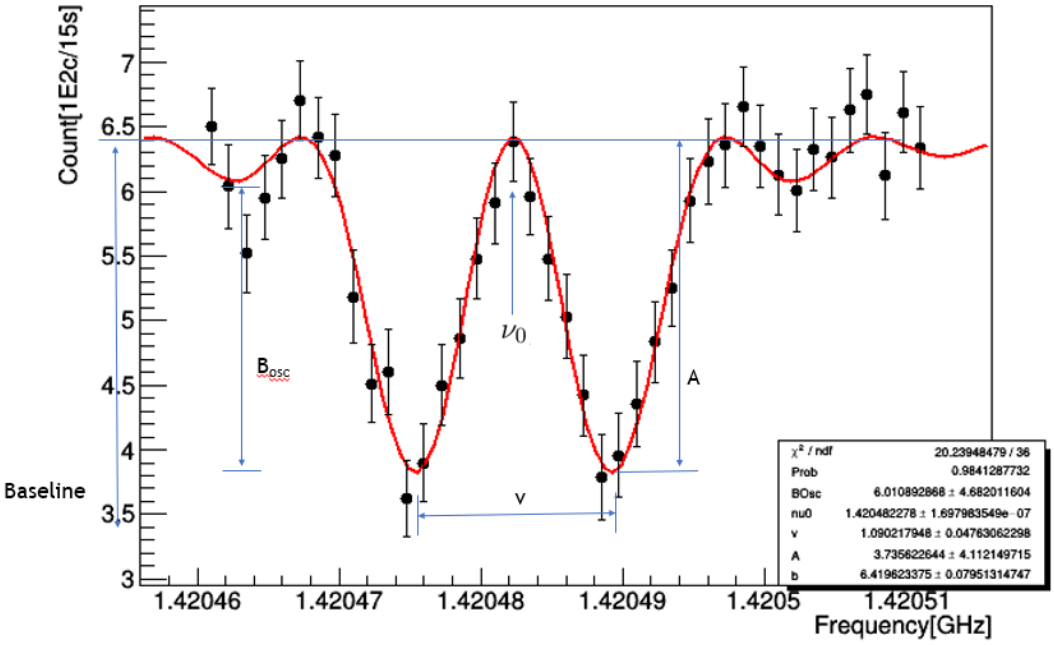

Figure 4.5: Example for a resonance fit with sketched effects on the shape by the parameters.

different. The apertures select a radius where the velocities of the two states are close but not equal (fig. 4.6).

The velocity within one set is stable which can be seen in fig. 4.7. The fixing happens for every set and transition separately calculating the weighted mean of the velocity.

The fixing could have also been done using one fixed velocity value for all sets. The weighted means of the measurement and the simulated results are given in table 4.2.

Table 4.2: Beam velocity results of the measurement and simulation done in [9].

Velocity	Measurement $\frac{\mathrm{m}}{\mathrm{s}}$	Simulation $\frac{\mathrm{m}}{\mathrm{s}}$
v_σ	1001.7 ± 1.7	974.1
v_π	1073.6 ± 1.9	1040.4

The small difference between the measured and the simulated velocities can be explained by idealistic conditions in the simulation.

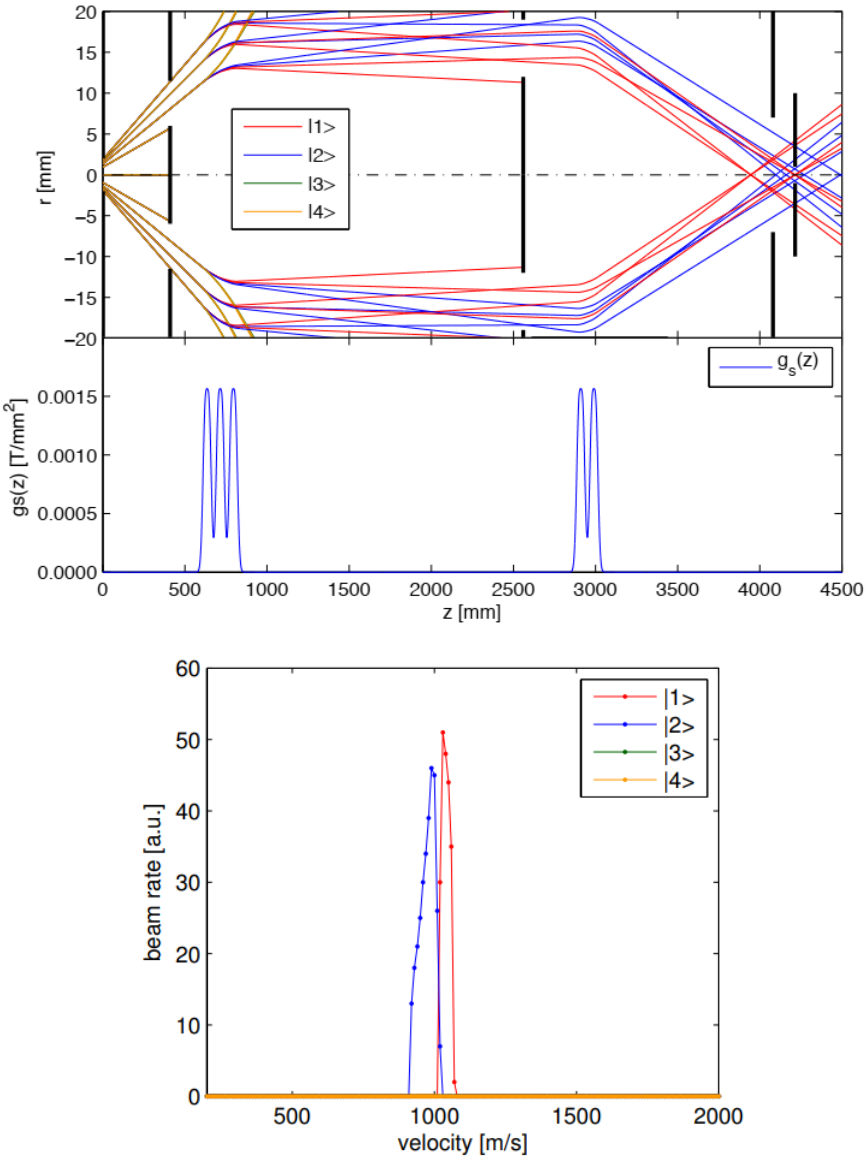

Figure 4.6: Top: Simulation of the trajectories of the atoms passing the polarising magnets, the apertures and the analysing magnets.
Bottom: Simulation of the velocity of the different states to reach the detector. State $|3\rangle$ and $|4\rangle$ do not reach the detector at all and the velocity of state $|1\rangle$ and $|2\rangle$ have to be different. From [9].

Oscillating magnetic field

The oscillating magnetic field to trigger the transition has to be different for the π- and σ-transition which was derived in chapter 2.2.2. Because of this the π- and the σ-transition data are split for the evaluation (fig. 4.8). Missing points in the plots are taken out of the analysis because of problems with the data acquisition - wrong frequency range scanned and because of this no resonance could be observed - or with the fit. The fixing of the magnetic field is done by calculating the weighted mean of all cycles for one set. Afterwards the resonance fit is repeated with velocity and oscillating

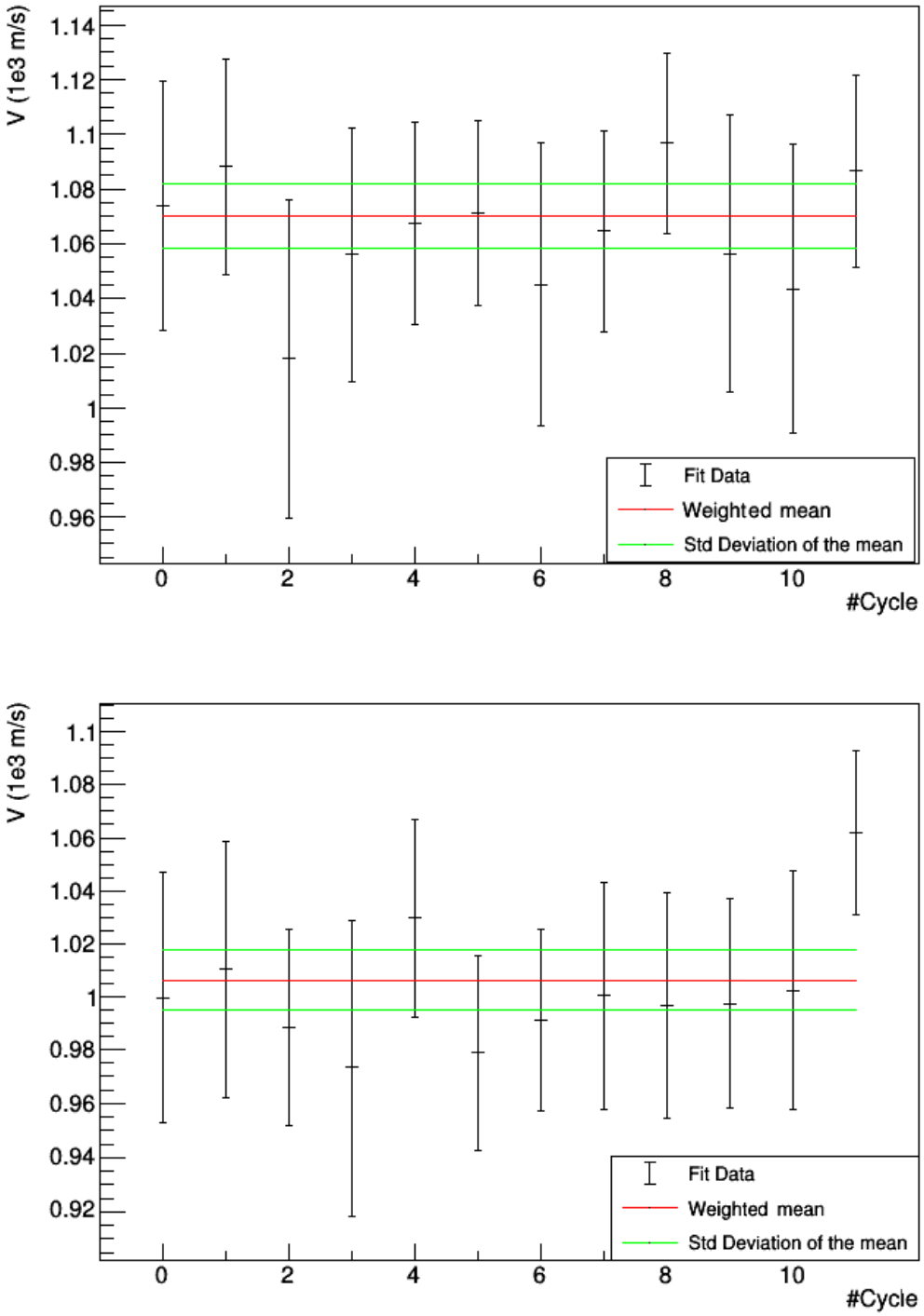

Figure 4.7: Top: Beam velocity result of the $|1\rangle$-state of set 4 of the second half of October LT data.
Bottom: Beam velocity result of the $|2\rangle$-transition of set 4 of second half of October LT data.

magnetic field fixed to the average of the set and it is compared to the resonance fit with free parameters.

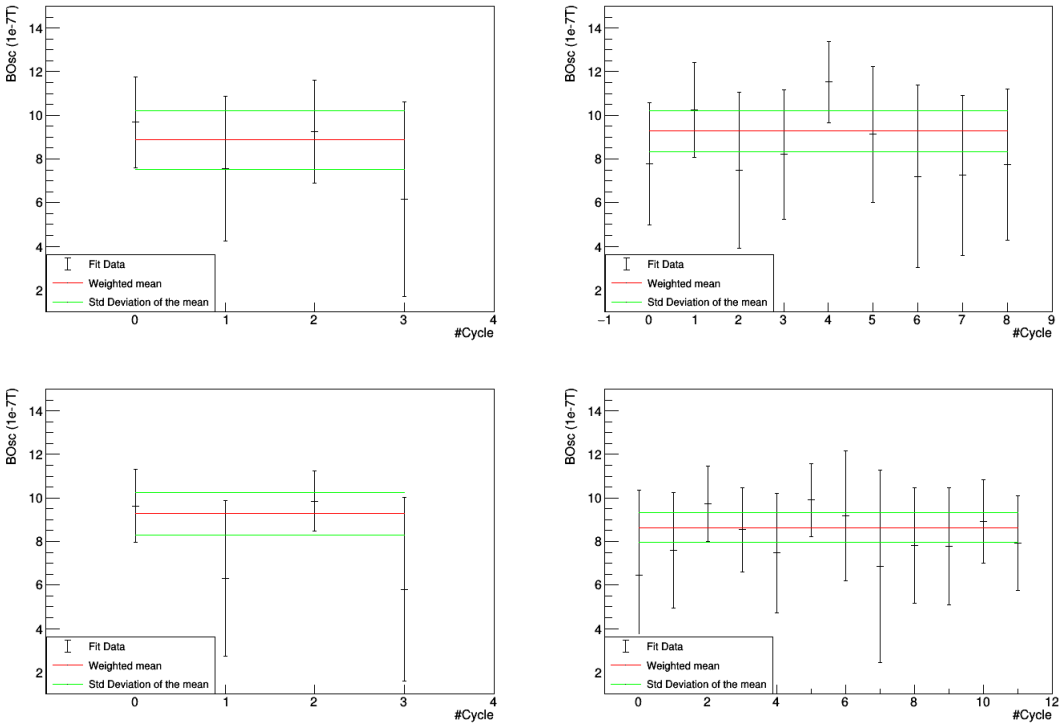

Figure 4.8: Weighted mean of the oscillating magnetic field for the π-transition at 1.9 A (Top left), without 1.9 A (Top right), σ-transition at 1.9 A (Bottom left) and without 1.9 A (Bottom right) for set 1 of October LT data.

For the oscillating magnetic field the weighted means have to be treated separately. For February the oscillating magnetic field for the σ-transition is

$$Feb.\ \sigma: \quad B_{\text{osc}} = (8.60 \pm 0.16) \cdot 10^{-7}\,\text{T} \tag{4.4}$$

For the π-transition the fitted oscillating magnetic field values have to be multiplied by a factor $\sqrt{2}$ as it was derived in section 2.2.2 at zero magnetic field. The bivariate spline is based on calculations of the σ-transition probability from which the oscillating magnetic field for the π-transition differs by this factor. The calculated weighted mean is

$$Feb.\ \pi: \quad B_{\text{osc}} = (14.41 \pm 0.17) \cdot 10^{-7}\,\text{T} \tag{4.5}$$

For the October data the oscillating magnetic field can be calculated for the 1.9 A cycles and the smaller magnetic field cycles separately, which gives for the σ-transition

$$\begin{aligned} Oct.\ \sigma\ without\ 1.9\,\text{A}: \quad & B_{\text{osc}} = (8.45 \pm 0.15) \cdot 10^{-7}\,\text{T} \\ Oct.\ \sigma\ at\ 1.9\,\text{A}: \quad & B_{\text{osc}} = (8.68 \pm 0.38) \cdot 10^{-7}\,\text{T} \end{aligned} \tag{4.6}$$

and for the π-transition

$$\begin{aligned} Oct.\ \pi\ without\ 1.9\,\mathrm{A}: &\quad B_{\mathrm{osc}} = (13.07 \pm 0.28) \cdot 10^{-7}\,\mathrm{T} \\ Oct.\ \pi\ at\ 1.9\,\mathrm{A}: &\quad B_{\mathrm{osc}} = (12.66 \pm 0.82) \cdot 10^{-7}\,\mathrm{T} \end{aligned} \tag{4.7}$$

4.3 Determination of the transition frequency at zero B-field

The transition frequency is calculated in three different ways

- Extrapolating the data for the σ-transition to zero static magnetic field
- Extrapolating the data for the π-transition to zero static magnetic field
- Calculating the transition frequency at zero static magnetic field from the π- and σ-transition at same magnetic field

4.3.1 Extrapolating the σ-transition

From each cycle the transition frequency at a given static magnetic field can be evaluated. The 12 cycles in the February and October ST data and the 16 cycles in the October LT data can be extrapolated to the transition frequency at zero magnetic field.

As derived in section 2.2.2 the Zeeman shifted frequency of the σ-transition can be calculated using

$$\nu_{\sigma_1} = \frac{E_2 - E_4}{h} = \nu_0 \sqrt{1 + \left(\frac{(g_I - g_J)\mu_{\mathrm{B}} B}{\nu_0 h} \right)^2}$$

For the fit the formula is simplified to

$$\nu_\sigma = \nu_0 \sqrt{1 + \tilde{B}^2} + 1.4(\sqrt{1 + \tilde{B}^2} - 1) \tag{4.8}$$

with a normalized $\tilde{B} = B_{real} \frac{(g_J - g_I)\mu_{\mathrm{B}}}{h\nu_0}$, $B_{real} = kI + B_{res}$, I is the coil current, B_{res} a residual magnetic field and k the constant of proportionality between the magnetic field and the current. The second term is introduced because from each frequency 1.4 GHz are subtracted to get smaller values. Two types of extrapolations are done: one time using all cycles and one time for the October LT data without using the 1.9 A cycles. Because of this the impact of the high magnetic field values to the whole evaluation can be investigated. Further, the transition frequency at zero magnetic field is extrapolated with the results for the central frequency of the resonance fit with free velocity and oscillating magnetic field and with fixed values of the velocity and oscillating magnetic field, described in subsection 4.2.1. Fig. 4.9 shows examples for the determination via

extrapolation of the σ-transition. It can be seen that the reduced $\chi^2 < 1$. This is because of the large error bars resulting from the resonance fit.

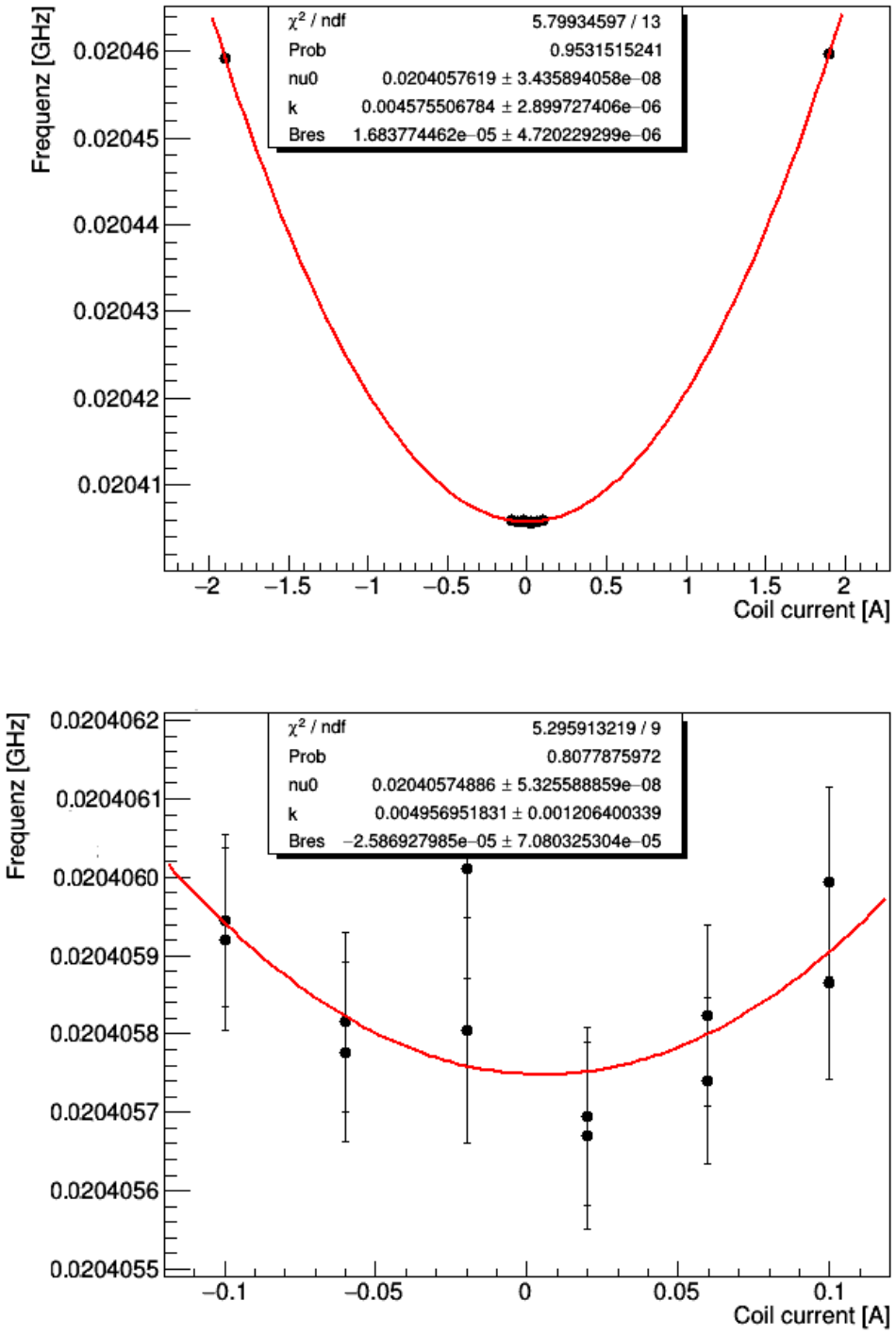

Figure 4.9: Top: σ-transition dependency on the static magnetic field of October LT data set 0.
Bottom: σ-transition dependency on the static magnetic field of October LT data set 0 without ± 1.9 A cycles. 1.4 GHz are subtracted from the value.

Looking at the transition frequency of free and fixed velocity and oscillating magnetic field it can be seen, that it does not have an impact on the result (top of fig. 4.10). Therefore further evaluations are done with fixed parameters. The σ-transition at low static magnetic field is not very sensitive to changes in the magnetic field and the zero-field value obtained from an extrapolation can only deviate marginally from the low field values. For the same reason the effect on the transition frequency is negligible when making the evaluation without the higher magnetic field cycles (bottom of fig. 4.10).

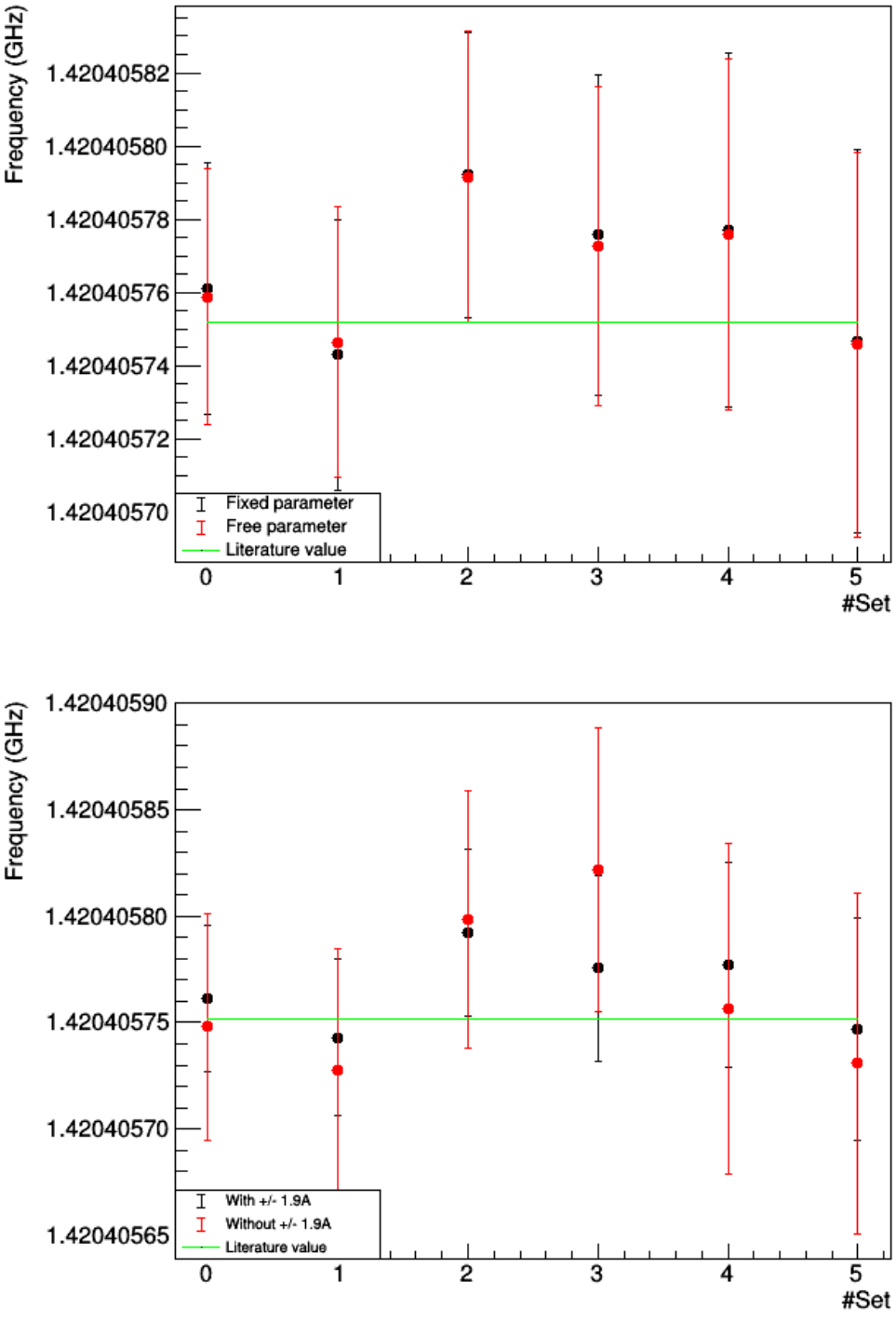

Figure 4.10: Top: Comparison of the σ-transition frequency by calculating it with free (red) respectively fixed (black) velocity and oscillating magnetic field.
Bottom: Comparison of the σ-transition frequency by calculating it with $\pm 1.9\,A$ cycles (black) respectively without $\pm 1.9\,A$ cycles (red).

4.3.2 Extrapolating the π-transition

The π-transition extrapolation is done the same way like the σ-extrapolation. Here the transition frequency is given by

$$\nu_{\pi_1} = \frac{E_1 - E_4}{h} = \frac{\nu_0}{2} + \frac{(g_J + g_I)\mu_B B}{2h} + \frac{\nu_0}{2}\sqrt{1 + \left(\frac{(g_I - g_J)\mu_B B}{\nu_0 h}\right)^2}$$

which gets modified to

$$\nu_\pi = \frac{\nu_0}{2}\big(1 + \sqrt{1 + \tilde{B}^2} + \frac{g_J + g_I}{g_J - g_I} \mid \tilde{B} \mid \big) + \frac{1.4}{2}\big(- 1 + \sqrt{1 + \tilde{B}^2} + \frac{g_J + g_I}{g_J - g_I} \mid \tilde{B} \mid \big) \quad (4.9)$$

The extrapolated π-transition is plotted in fig. 4.11. For the data evaluated by using all magnetic field values the reduced χ^2 is about 4.5. This is because the $\pm 1.9\,\mathrm{A}$ central frequencies do not shift as much as the smaller central frequencies (see next chapter) and hence the fit function can not describe the course of the measured points.

Again freeing and fixing velocity and oscillating magnetic field does not have a big effect on the result. The π-transition is sensitive to small changes of the magnetic field and therefore the 1.9 A cycles have a big impact on the result (fig. 4.12). The difference of the calculated values at small magnetic field from the literature value is explained in chapter 5.

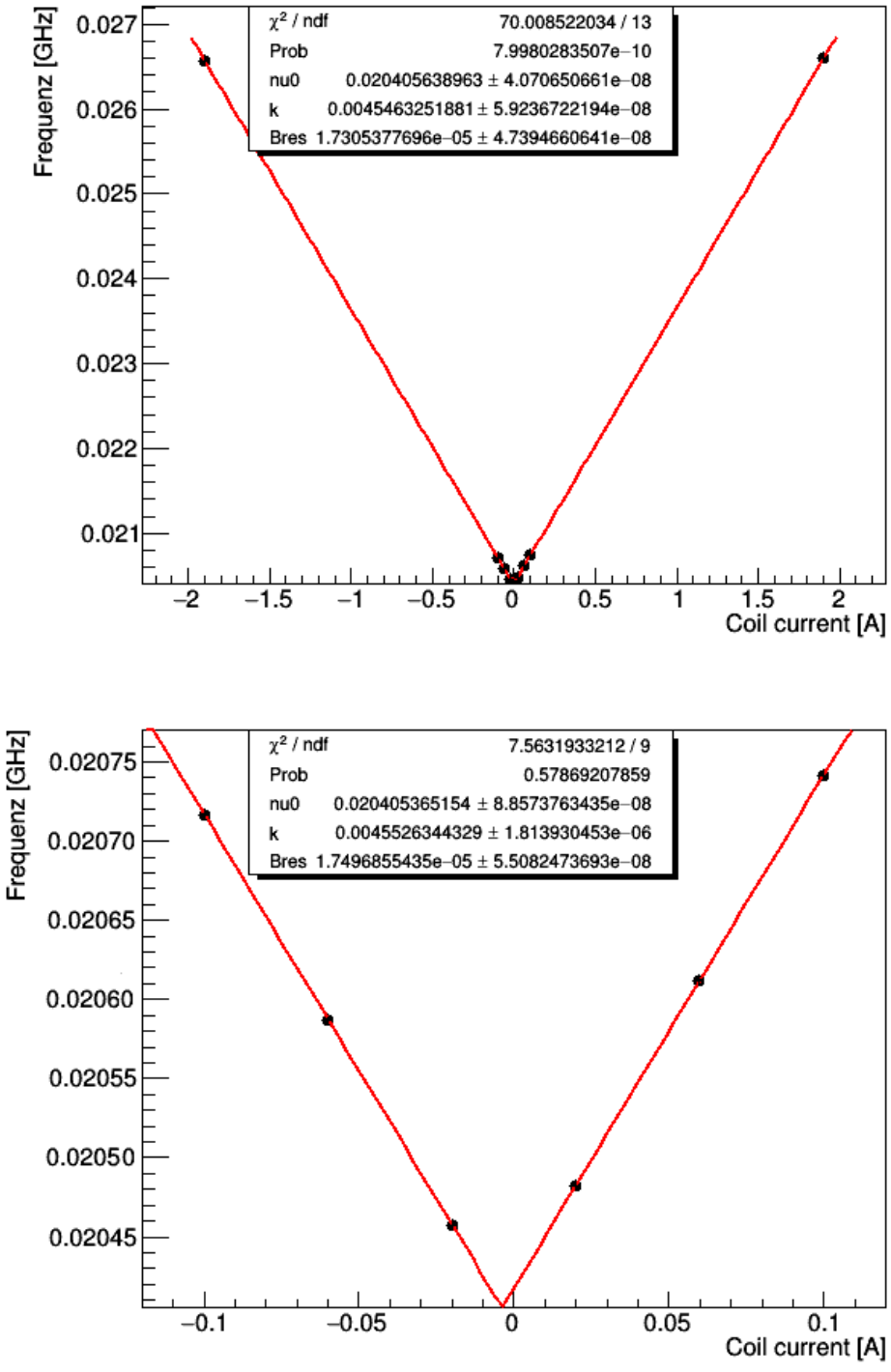

Figure 4.11: Top: π-transition dependency on the static magnetic field of October LT data set 0 with $\pm 1.9\,A$.
Bottom: π-transition dependency on the static magnetic field of October LT data set 0 without $\pm 1.9\,A$ cycles. 1.4 GHz is subtracted from the value.

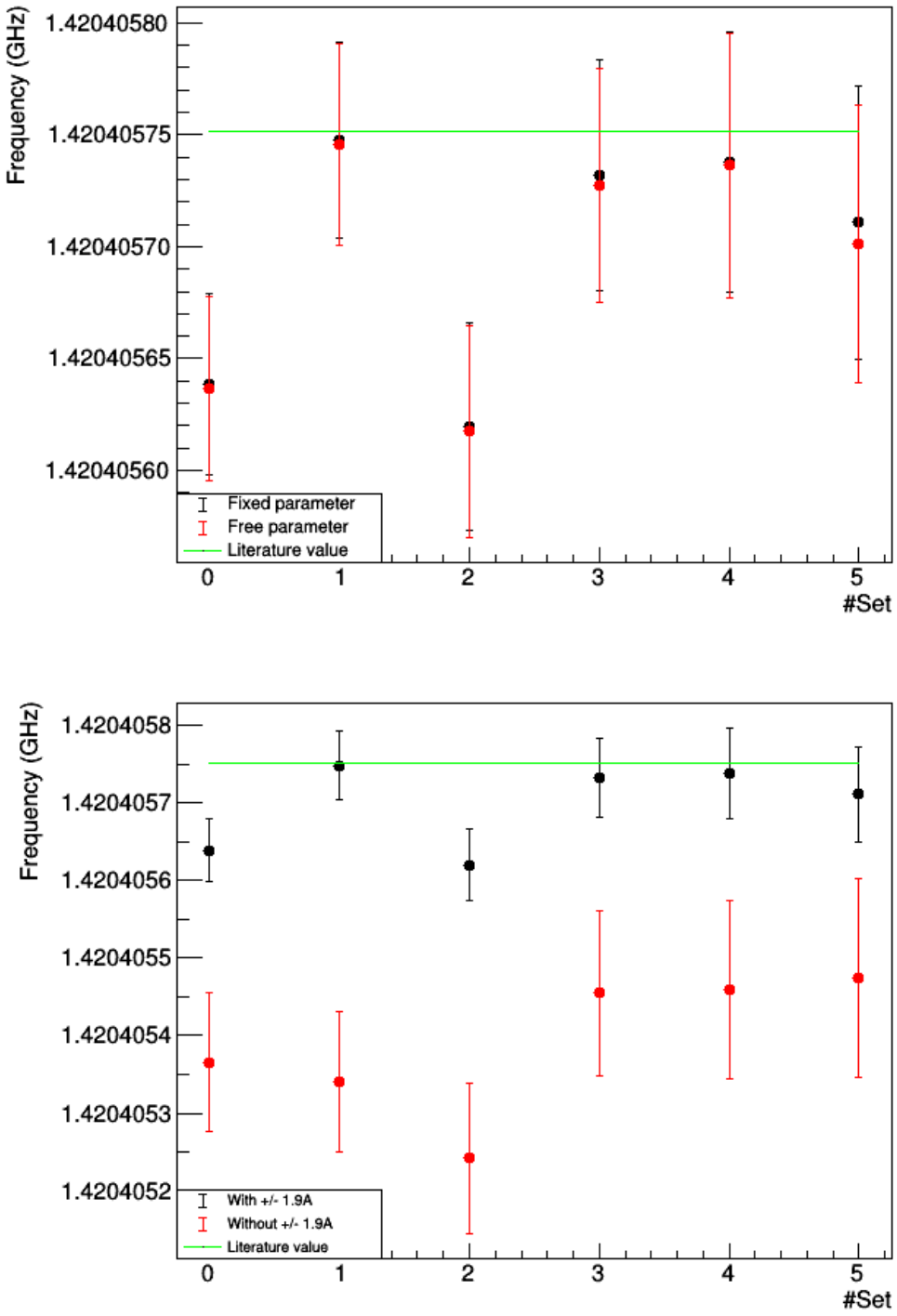

Figure 4.12: Top: Comparison of the π-transition for free (red) and fixed (black) velocity and oscillating magnetic field and their effect on the result for the second half of the October LT data. Bottom: Comparison of the evaluation with (black) and without (red) $\pm 1.9\,A$ cycles.

4.3.3 Calculation of the transition frequency using π- and σ-transition at same magnetic field

The third method to calculate the transition frequency at zero magnetic field is by using the π- and σ-measurement at the same magnetic field. Therefore the two equations to calculate the two transitions for a given magnetic field B are combined by eliminating B and solving for the zero-field value ν_0:

$$\nu_0 = \frac{g_- \sqrt{g_-^2 \nu_\sigma^2 - 4g_+^2 \nu_\pi^2 + 4g_+^2 \nu_\pi \nu_\sigma} + g_+^2 (2\nu_\pi - \nu_\sigma)}{g_+^2 - g_-^2} \tag{4.10}$$

with $g_+ = g_J + g_I$ and $g_- = g_J - g_I$. The advantage of this method is that it is independent of the static magnetic field. The only requirement is that the two transition frequencies are measured at exactly the same magnetic field.

With this method the cycles measured at the same magnetic field of each measurement period are evaluated to get six (for February data and October ST data) or eight (October LT) values for the transition frequency. These values are afterwards analysed to get one transition frequency for each period (fig. 4.13).

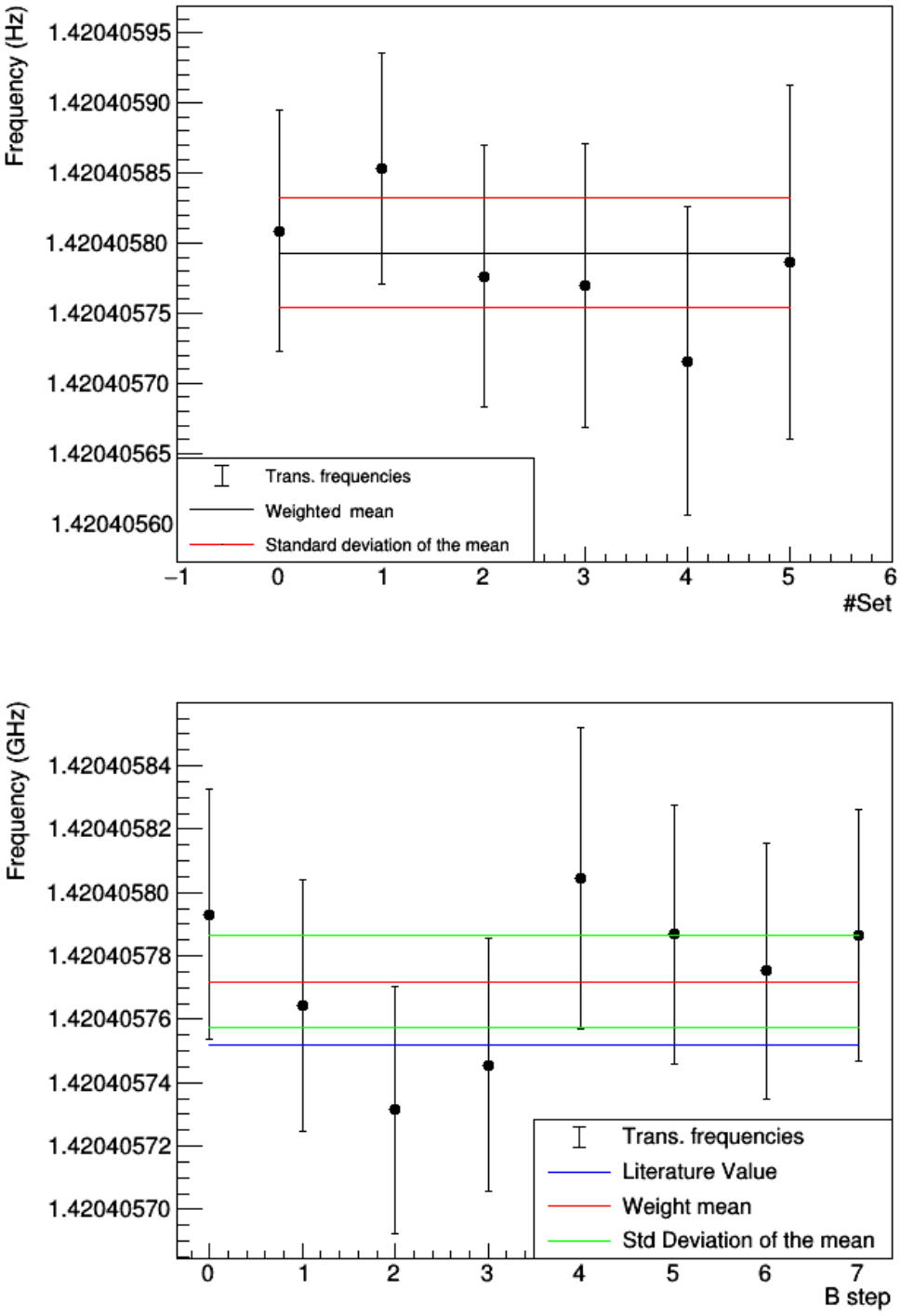

Figure 4.13: Plots of the transition frequency at zero magnetic field using π- and σ-transition at same magnetic field. Top: Calculation for 1.9 A coil current over all sets of the second half of the October LT data. Bottom: For each magnetic field value of October LT data. The y-axis should be seen as "B step 0 " = -1.9 A, "B step 1" = -0.1 A and so on.

Chapter 5

Correction

Looking at the π-transition frequency of the October data calculated for small static magnetic field, a difference of a few hundred of Hertz from the literature value can be seen in fig. 4.12. To explain this difference a correction is applied which is described in this chapter.

5.1 Reasons for the correction

The π-transition frequency depends strongly on the static magnetic field. Going to a higher magnetic field, the Zeeman-splitting gets wider and therefore the hyperfine splitting can be explained quite well by calculating a two-level system. Using a small magnetic field leads to a shift of the π-transition frequency (fig. 5.1).

It can be seen that the σ-transition probability is nearly unchanged but the π-transition probability deforms and shifts towards lower frequencies. This is because the fit function for the resonance fit which is used is based on a two-level system. This function is symmetric around the central frequency which is not valid anymore because of the deformation, i.e. the used fit function does not account for the entire physics of the line-shape. To take this deviation into account the four-level system has to be solved.

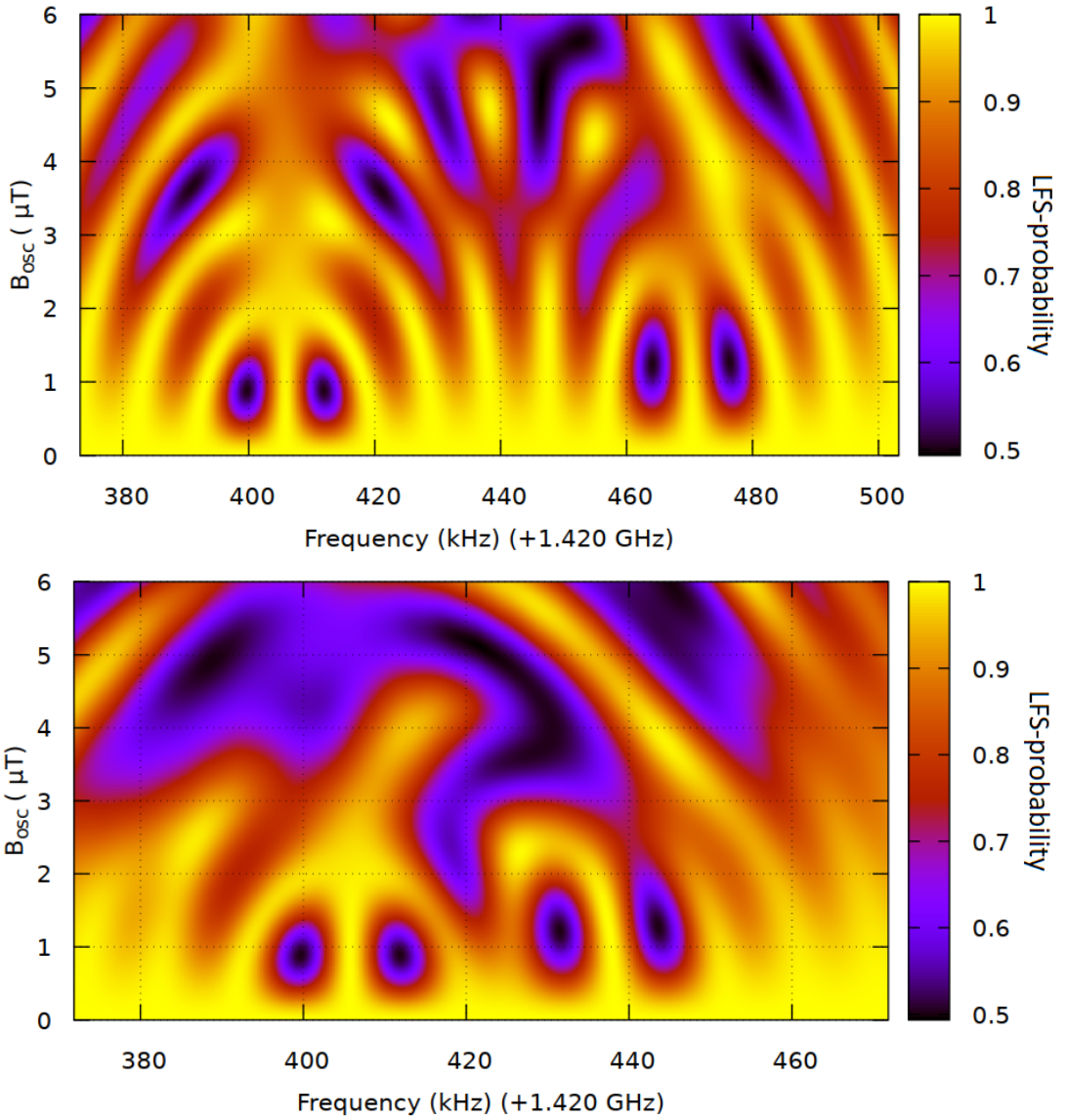

Figure 5.1: Simulation of the dependence of the transition probability on the oscillating magnetic field amplitude and the frequency at a static magnetic field of 46 mG (Top) and 23 mG (Bottom). Made by Duc Phan Than.

5.2 Details of the Correction

The correction is done by using the evaluated results to check if a four-level system could explain the shift. The procedure for doing this is as follows

- Calculating the magnetic field value from the π-transition central frequency of the resonance fits.
- Generating fake data by solving the four-level system at the given magnetic field.
- Performing a fit on the fake data based on the two-level system line shape to retrieve the shift of the central frequency as the difference between the transition frequency entering the four-level system calculation and the fit result.

- Applying this systematic shift to the real data as a correction.

- Determining the zero-field transition frequency using the corrected data.

5.2.1 Magnetic field and fake data

The π-transition is very sensitive to changes in the magnetic field. The central frequency can be used to extract the magnetic field value quite exactly by using

$$B_{\text{stat}} = \frac{K_1(2\nu_0 - \nu_{\text{lit}}) - \sqrt{K_1^2\nu_{\text{lit}}^2 + 4K_2\nu_0(\nu_0 - \nu_{\text{lit}})}}{K_1^2 - K_2} \tag{5.1}$$

with $K_1 = -(g_J + g_I)\frac{\mu_B}{h}$, $K_2 = \left((g_J - g_I)\frac{\mu_B}{h}\right)^2$, ν_0 the central frequency and ν_{lit} the literature value of the transition frequency at zero magnetic field.

The fake data at this magnetic field are generated by solving the von Neuman equation of chapter 2.2.2. At first the transition frequencies at the extracted magnetic field are calculated to obtain the transition frequency matrix $T_{ij} = 2\pi(\nu_i - \nu_j) = \omega_{ij}$ $(i, j = 1, ..., 4)$. The density matrix is initialised for a completely polarised beam with $50\% : 50\%$ sharing between the two LFS states

$$\rho(0) = \begin{pmatrix} 0.5 & 0 & 0 & 0 \\ 0 & 0.5 & 0 & 0 \\ 0 & 0 & 0 & 0 \\ 0 & 0 & 0 & 0 \end{pmatrix} \tag{5.2}$$

The von Neumann equation is solved by using the Heun method. Therefore the initial Hamiltonian is calculated to

$$H_{XZ} = \sin(\theta_B)H_X + \cos(\theta_B)H_Z \tag{5.3}$$

with θ_B is the angle between the static and oscillating magnetic field, H_X the Hamiltonian for an oscillating B-field pointing in x-direction and H_Z the Hamiltonian for an oscillating B-field pointing in z-direction. Explicitly the components of the Hamiltonian are

$$H_X = \tag{5.4}$$
$$= \begin{pmatrix} 0 & c_E\sin\theta + c_P\cos\theta & -c_E\cos\theta + c_P\sin\theta & 0 \\ c_E\sin\theta + c_P\cos\theta & 0 & 0 & c_E\cos\theta + c_P\sin\theta \\ -c_E\cos\theta + c_P\sin\theta & 0 & 0 & c_E\sin\theta - c_P\cos\theta \\ 0 & c_E\cos\theta + c_P\sin\theta & c_E\sin\theta - c_P\cos\theta & 0 \end{pmatrix}$$

with $c_E = \frac{1}{2}g_E\mu_B$, $c_P = \frac{1}{2}g_P\mu_N$ and θ the B-field dependent mixing angle and

$$H_Z = \begin{pmatrix} \mu & 0 & 0 & 0 \\ 0 & -\mu'(\cos\theta^2 - \sin\theta^2) & -\mu' 2\cos\theta\sin\theta & 0 \\ 0 & -\mu' 2\cos\theta\sin\theta & -\mu'(\cos\theta^2 - \sin\theta^2) & 0 \\ 0 & 0 & 0 & \mu \end{pmatrix} \tag{5.5}$$

with $\mu = -\frac{1}{2}\big(g_E\mu_\mathrm{B} + g_P\mu_N\big)$ and $\mu' = -\frac{1}{2}\big(g_E\mu_\mathrm{B} - g_P\mu_N\big)$. To solve the von Neumann equation

$$\frac{d\rho}{dt} = \frac{i}{\hbar}\big[H, \rho\big] \tag{5.6}$$

the Heun method is used. Calculating

$$k_1 = \frac{idt}{\hbar}\big[H_l, \rho_l\big] B_\mathrm{osc} \cos\big(\frac{z\pi}{L}\big) \cos(\omega t_l) \tag{5.7}$$

and

$$k_2 = \frac{idt}{\hbar}\big[dH_{l+1}, \rho_l + k_1\big] B_\mathrm{osc} \cos\big(\frac{z\pi}{L}\big) \cos(\omega t_{l+1}) \tag{5.8}$$

the iteration step $l+1$ is given by

$$\rho_{l+1} = \rho_l + \frac{1}{2}\big(k_1 + k_2\big) \tag{5.9}$$

with $H_{ij,l} = H_{ij}^{xz} e^{i\omega t_l}$ and $dH_{ij,l+1} = H_{ij}^{xz} e^{i\omega dt}$, L is the cavity length, z the position in the cavity and $t_{l+1} = t_l + dt$.

The transition probability of interest is then given by the sum $\rho_{11} + \rho_{22}$ which is the probability of having the hydrogen in one of the initial states.

5.2.2 Resonance fit and difference

The fake data generated as described in the previous subsection are fitted with the same function as the real data i.e. a symmetric function based on the two-level system. Therefore a shift is expected at lower magnetic field. The plots of the fitted fake data are shown for σ in fig. 5.2 and for π in fig. 5.3. The error used for the fake data is generated to get a reduced χ^2 of 1 for the cycle at highest magnetic field. For the central frequency the fit function looks quite accurate but the goal is to determine the central frequency at a line width of 12 kHz with a precision of 1 Hz.

The theoretical values for the central frequency calculated by solving the four-level system differ from the fitted central frequencies dependent on the static magnetic field. While at small magnetic fields the difference is quite high it gets smaller at high magnetic fields. The behaviour of the shift for the measured data as well for some idealised data is shown fig. 5.4.

The theoretical difference (red dots in fig. 5.4, the red curve connects the points to guide the eye) is calculated in an idealized picture with the exact magnetic field

without any residual B-field in x-direction - the constant of proportionality is given by $k = 2.3147 \cdot 10^{-4} \frac{\mathrm{T}}{\mathrm{A}}$. One oscillating magnetic field of the October data of $B_{\mathrm{osc}} = 13.07 \cdot 10^{-7}\,\mathrm{T}$ and a velocity of $v = 1040.4 \frac{\mathrm{m}}{\mathrm{s}}$, which is the idealistic result for the velocity simulation in [9]. The transition is then calculated by solving the four-level system. The resonance fit is afterwards done in a frequency range set symmetric around the central frequency. This idealization for the calculation is the reason of the deviation between the theoretical calculated shifts and the shifts from the data.

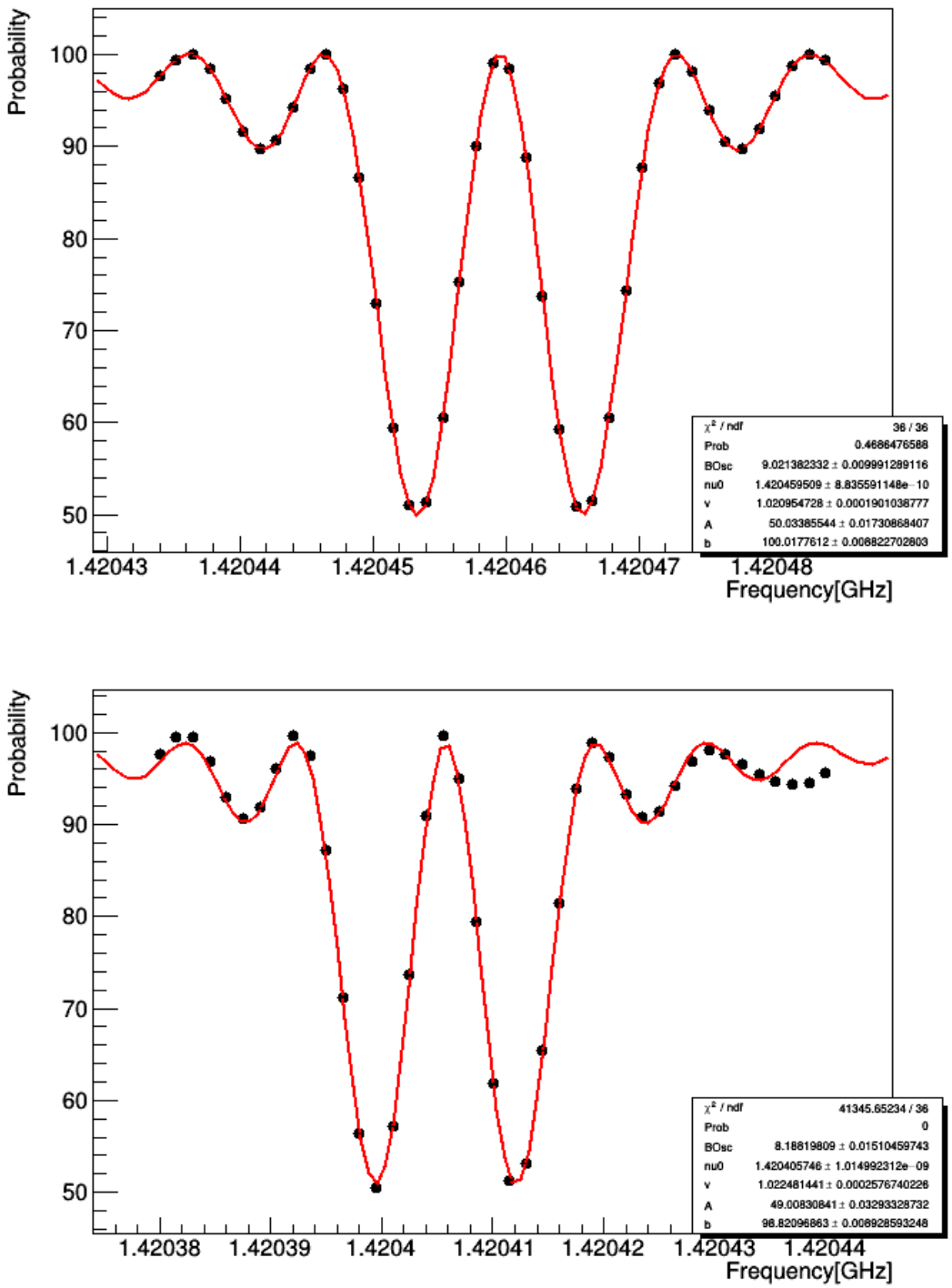

Figure 5.2: Two-level resonance fit of four-level fake data for σ-transition at -1.9 A (Top) and 0.02 A (Bottom) of October LT2 data.

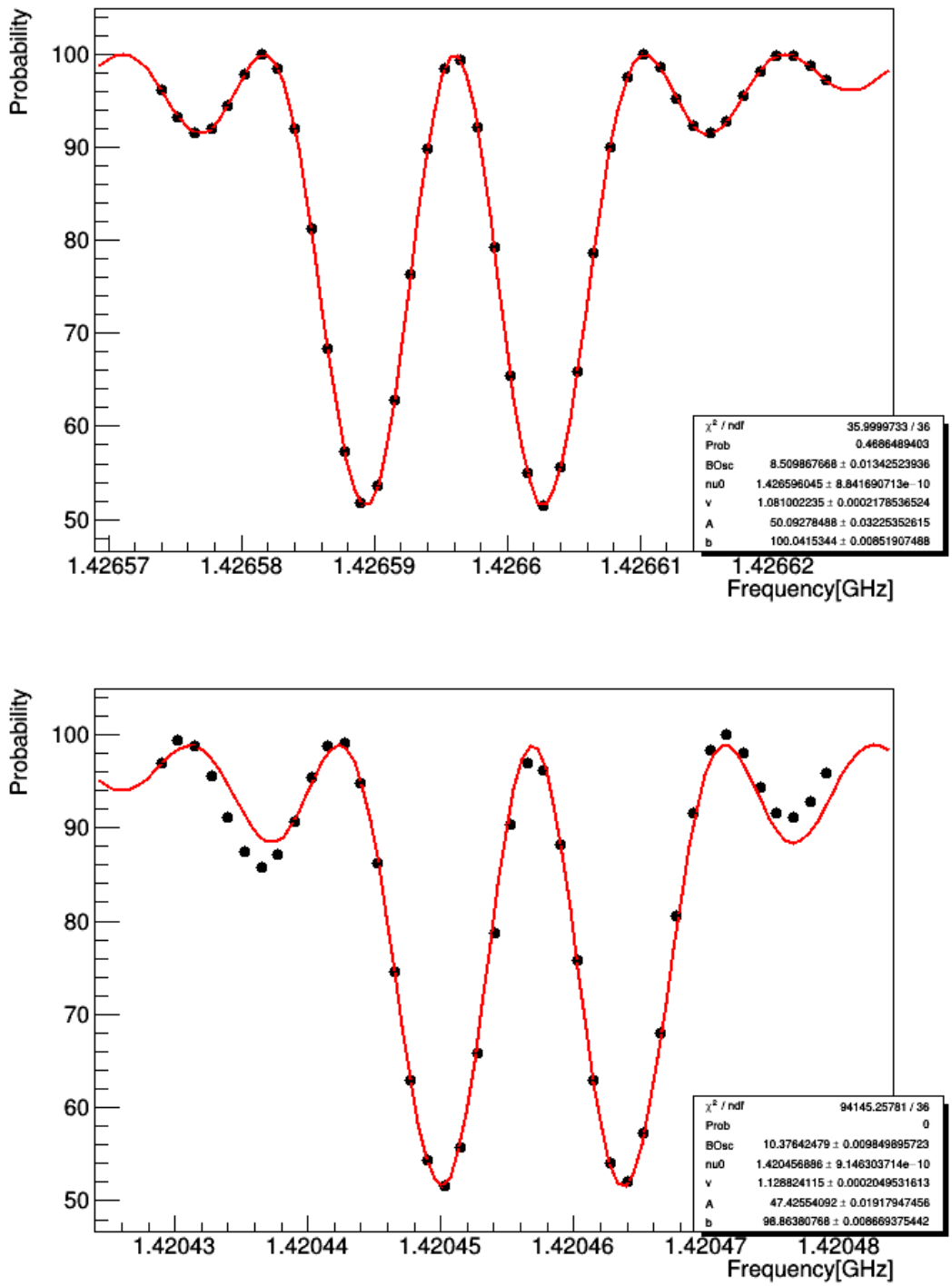

Figure 5.3: Two-level resonance fit of four-level fake data for π-transition at -1.9 A (Top) and 0.02 A (Bottom) of October LT2 data.

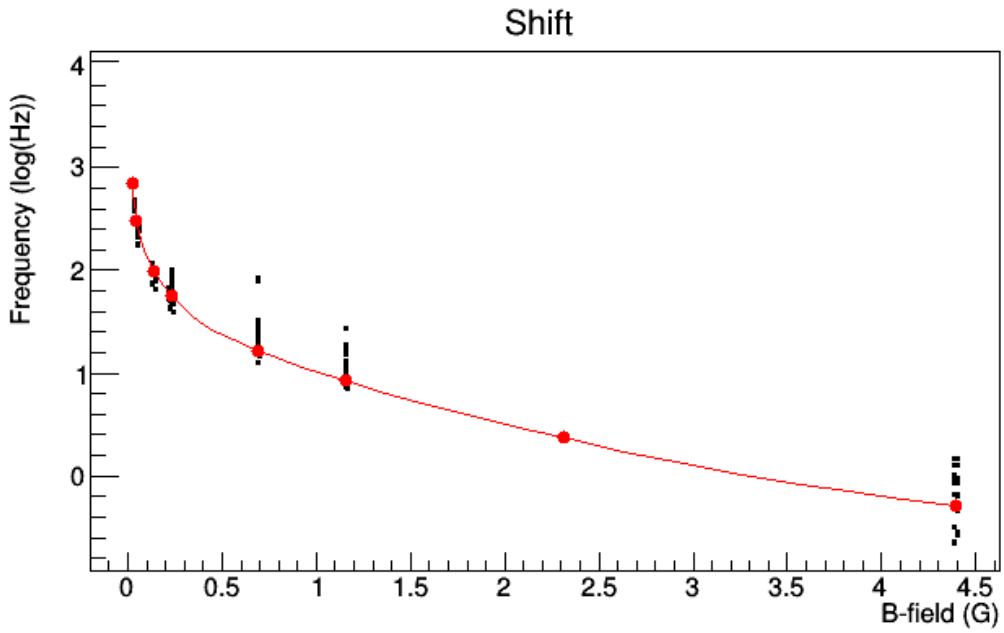

Figure 5.4: Difference between four-level calculated central frequencies and two-level fit result for the central frequencies depending on the static magnetic field for theoretical values (red dots) and measured values (black blocks). The red line connects the points to guide the eye. The theoretical values are calculated by using $B_{\mathrm{osc}} = 13.07 \cdot 10^{-7}\,\mathrm{T}$*, which is the fit result of the October data, and* $k = 2.3147 \cdot 10^{-4}\,\frac{\mathrm{T}}{\mathrm{A}}$ *which is the weight mean of the October LT2 data.*

5.2.3 Calculation of the transition frequency

The difference calculated in the last section is now used to correct the data. Therefore the shifts are applied to the fitted central frequencies of the real data. With this corrected data the zero-field transition frequency is calculated again using the three methods described in section 4.3.

The uncertainty of the corrected values is calculated using four terms:

- uncertainty of the central frequency of the real data resonance fit: $\sigma_{\text{real fit}}$
- uncertainty of the central frequency of the fake data resonance fit: $\sigma_{\text{fake fit}}$
- change of the central frequency of the fake data resonance fit evaluated at an oscillating magnetic field of $B_{\text{osc}} + \sigma_B$ respectively $B_{\text{osc}} - \sigma_B$ with σ_B is the standard deviation of the oscillating magnetic field: $\sigma_{\Delta B}$
- change of the central frequency of the fake data resonance fit evaluated with a velocity of $v + 3\sigma_v$ respectively $v - 3\sigma_v$ with σ_v is the standard deviation of the velocity: $\sigma_{\Delta v}$

The errors for each central frequency is then calculated by

$$\sigma_{\nu_C} = \sqrt{\sigma^2_{\text{real fit}} + \sigma^2_{\text{fake fit}} + \sigma^2_{\Delta B} + \sigma^2_{\Delta v}} \tag{5.10}$$

The contribution of the changes in velocity are in order of Hz while the oscillating magnetic field value has a bigger impact of a few ten Hz. The uncertainty of the real data is about 100-200 Hz while the fake data uncertainty is strongly dependent on the magnetic field value. For big magnetic field values the uncertainty is about 1 Hz and even less but at low magnetic field values it is a few hundreds of Hertz. This comes from the fact that there is just a small effect of the correction at high magnetic field values and it gets more effective at low magnetic fields.

The effect of the correction can be seen in fig. 5.5 and fig. 5.6. For the σ-transition the effect is rather small which fits to the theory as it is not quite sensitive to changes at small magnetic fields. The π-transition at small magnetic field is shifted towards the literature value. For the third method to calculate the zero magnetic field transition frequency the effect is negligible as it is magnetic field independent (fig. 5.7).

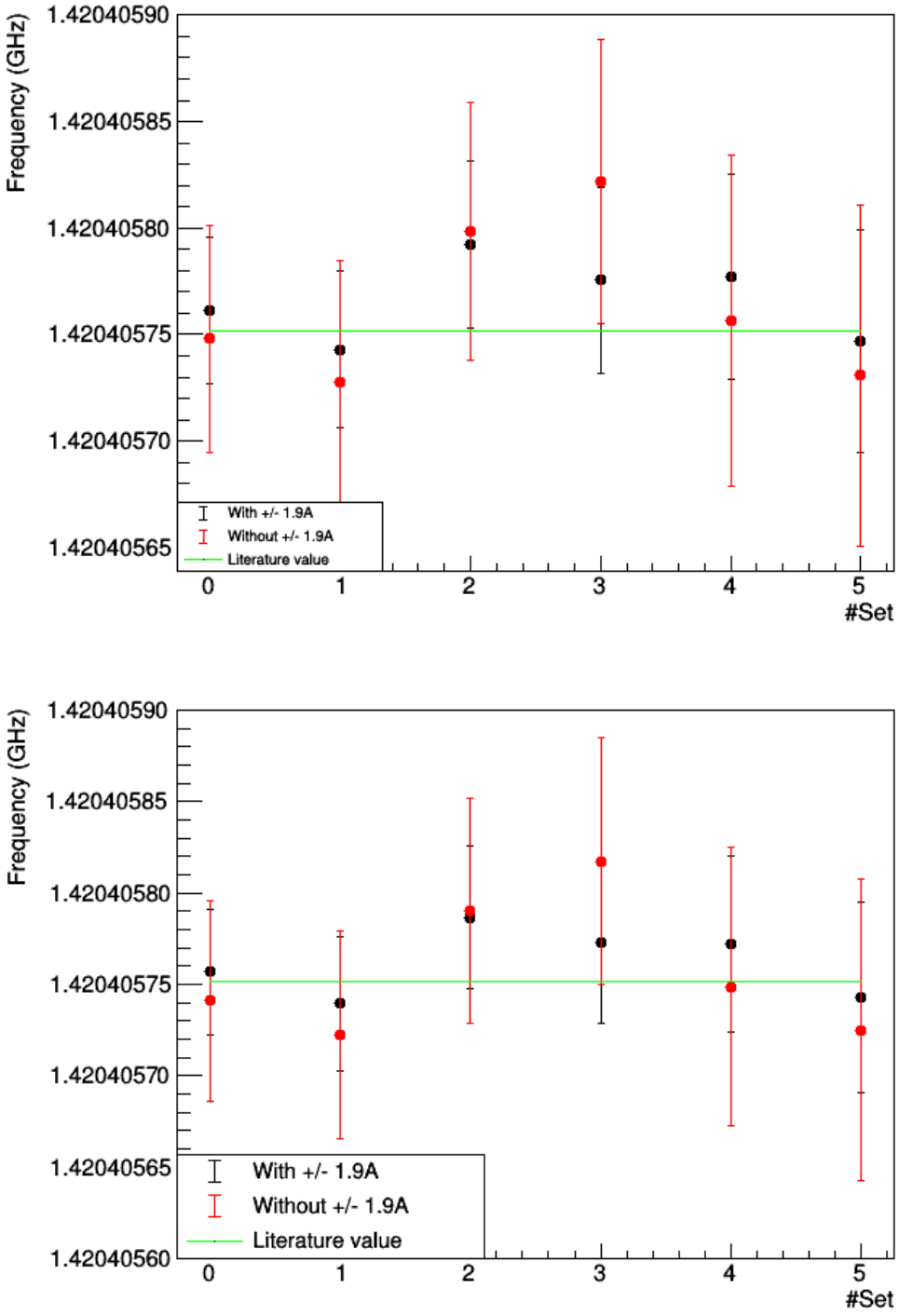

Figure 5.5: Effect of the correction for σ-transition. Transition frequency of October data before (Top) and after (Bottom) the correction.

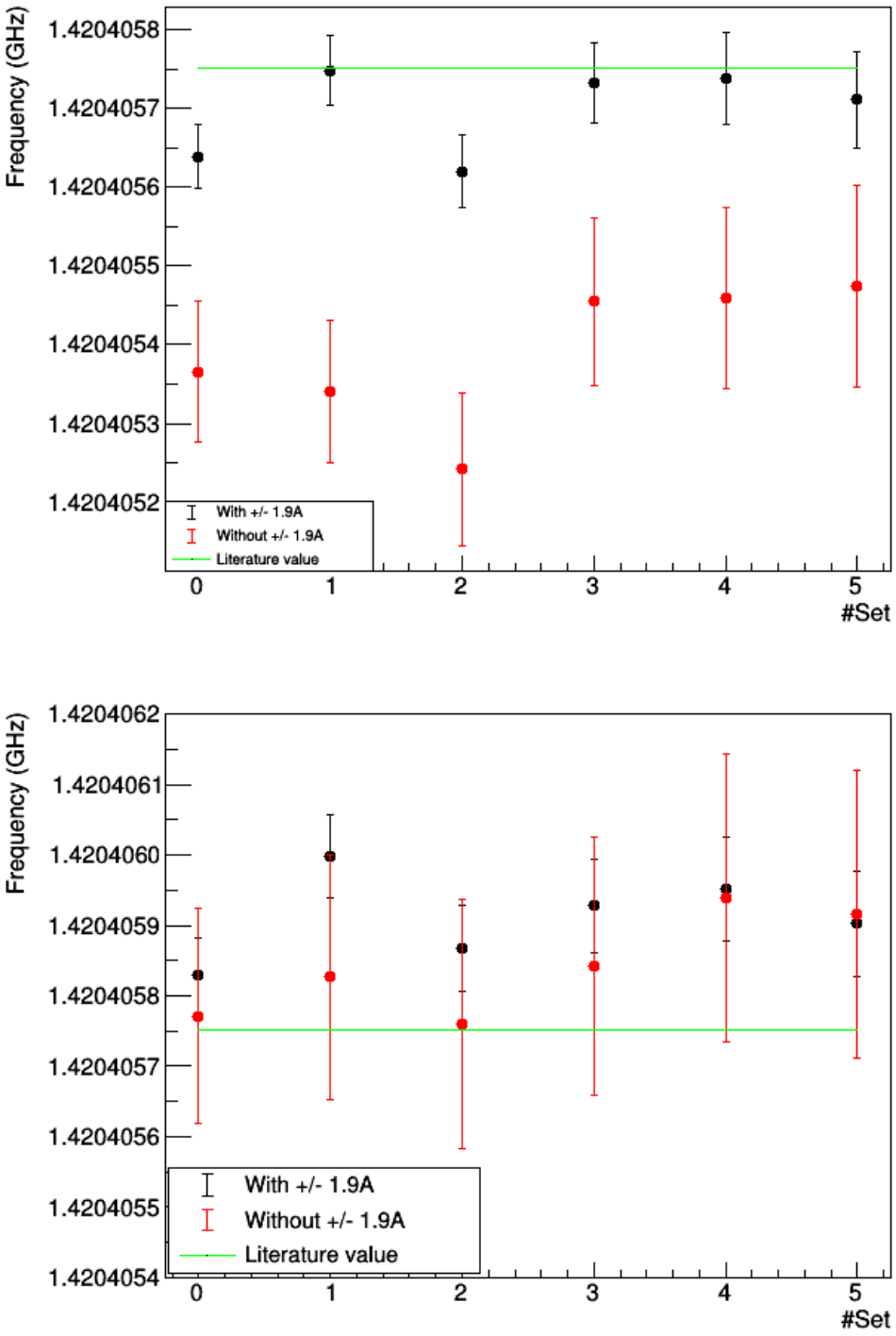

Figure 5.6: Effect of the correction for π-transition. Transition frequency of October data before (Top) and after (Bottom) the correction. The correction shifts the zero-field transition frequency to higher values which is discussed in subchapter 6.3.

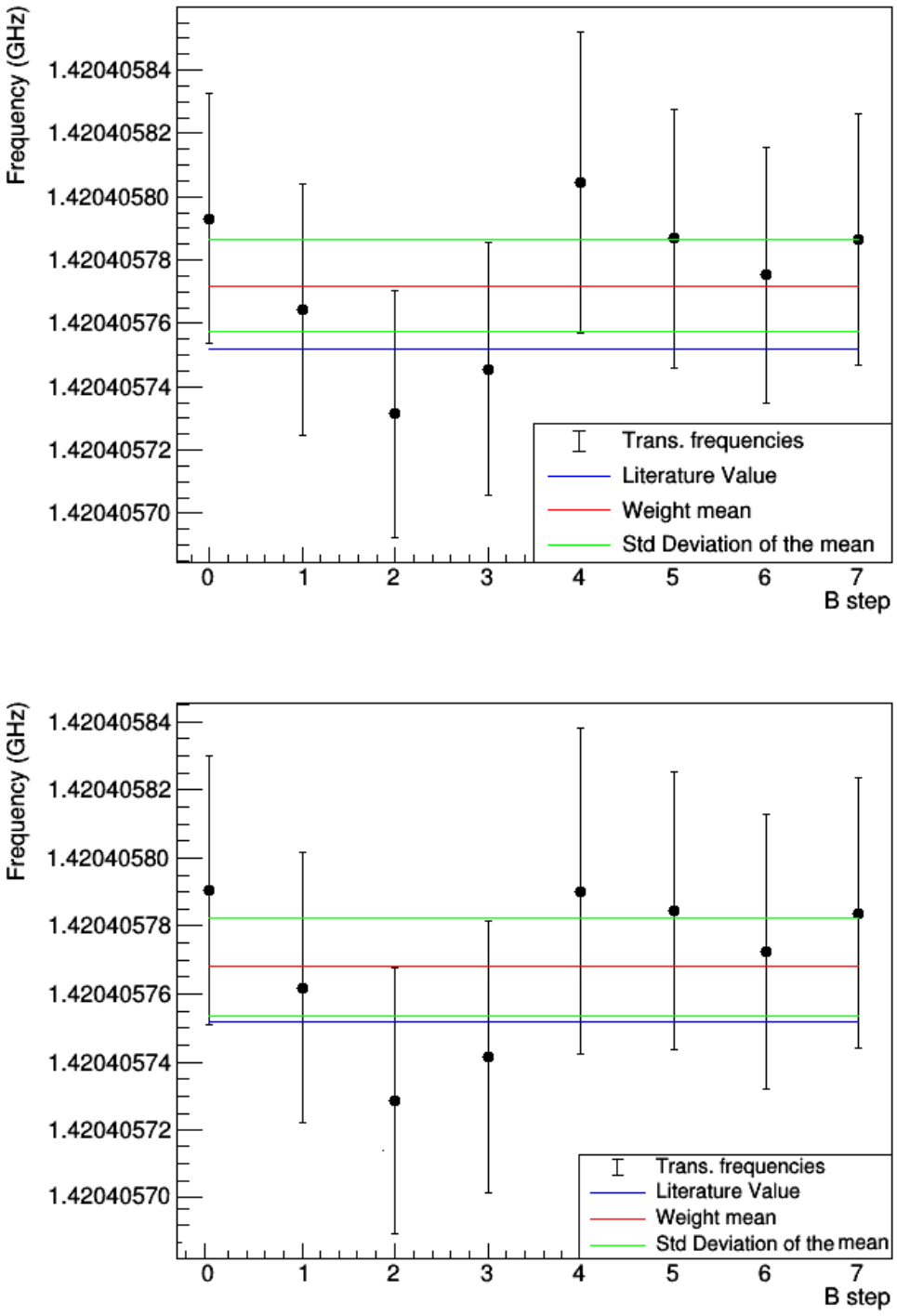

Figure 5.7: Effect of the correction for the transition frequency calculated by using π- and σ-transition at same magnetic field. Transition frequency of October data before (Top) and after (Bottom) the correction

Chapter 6

Results

As a consequence of the different static magnetic field values at which the frequencies are measured, the evaluation and thus the results are done for each measuring period separately. The results of the evaluation and the following correction are summarized in this chapter.

6.1 February data

The February data are measured at a magnetic field of ±0.231 G, ±0.944 G and ±1.157 G. All together there are 27 sets evaluated. The transition frequency of each set is listed in table 8.2 in the appendix. With these sets weighted means can be calculated which are listed in table 6.1.

Table 6.1: Results of the hyperfine transition of the February data and its deviation from the literature value $\nu_{\mathrm{lit}} = 1420405752\,\mathrm{Hz}$

Transition	Uncorrected (Hz)	$\nu_0 - \nu_{\mathrm{lit}}$ (Hz)	Corrected (Hz)	$\nu_{0,\mathrm{corr}} - \nu_{\mathrm{lit}}$ (Hz)
ν_σ	1420405758 ± 16	6 ± 16	1420405755 ± 25	3 ± 25
ν_π	1420405736 ± 23	-16 ± 23	1420405813 ± 25	61 ± 25
Same B	1420405756 ± 11	4 ± 11	1420405754 ± 11	2 ± 11

The π- and the σ-transition calculated by extrapolating to zero magnetic field can be combined as they use independent data. This yields

$$\nu_0 = (1420405751 \pm 14)\,\mathrm{Hz} \tag{6.1}$$

which deviates -1 Hz from the literature value and has a relative precision of $9.9{\cdot}10^{-9}$.

6.2 October data

The October data are measured at a magnetic field of ±0.231 G, ±0.139 G and ±0.046 G. Additionally in the October LT data the point ±4.398 G is measured. The results for

October are listed in table 6.2, 6.3 and 6.4. The transition frequencies of each set is shown in table 8.3 - 8.5 in the appendix.

Table 6.2: Results of the hyperfine transition of the October Short Term data and its deviation from the literature value $\nu_{\mathrm{lit}} = 1420405752\,\mathrm{Hz}$.

Transition	Uncorrected (Hz)	$\nu_0 - \nu_{\mathrm{lit}}$ (Hz)	Corrected (Hz)	$\nu_{0,\mathrm{corr}} - \nu_{\mathrm{lit}}$ (Hz)
ν_σ	1420405772 ± 20	14 ± 20	1420405756 ± 21	4 ± 21
ν_π	1420405169 ± 38	-583 ± 38	1420405653 ± 80	-99 ± 80
Same B	1420405772 ± 13	20 ± 13	1420405766 ± 13	14 ± 13

Table 6.3: Results of the hyperfine transition of the October Long Term 1 data and its deviation from the literature value $\nu_{\mathrm{lit}} = 1420405752\,\mathrm{Hz}$.

Transition	Uncorrected (Hz)	$\nu_0 - \nu_{\mathrm{lit}}$ (Hz)	Corrected (Hz)	$\nu_{0,\mathrm{corr}} - \nu_{\mathrm{lit}}$ (Hz)
$\nu_{\sigma,smallB}$	1420405762 ± 21	10 ± 21	1420405758 ± 21	6 ± 21
$\nu_{\sigma,allB}$	1420405774 ± 13	22 ± 13	1420405772 ± 13	20 ± 13
$\nu_{\pi,smallB}$	1420405469 ± 55	-283 ± 55	1420405787 ± 73	35 ± 73
$\nu_{\pi,allB}$	1420405825 ± 20	73 ± 20	1420405924 ± 23	172 ± 23
Same B	1420405772 ± 15	19 ± 12	1420405772 ± 15	17 ± 12

Table 6.4: Results of the hyperfine transition of the October Long Term 2 data and its deviation from the literature value $\nu_{\mathrm{lit}} = 1420405752\,\mathrm{Hz}$.

Transition	Uncorrected (Hz)	$\nu_0 - \nu_{\mathrm{lit}}$ (Hz)	Corrected (Hz)	$\nu_{0,\mathrm{corr}} - \nu_{\mathrm{lit}}$ (Hz)
$\nu_{\sigma,smallB}$	1420405764 ± 27	12 ± 27	1420405757 ± 27	5 ± 27
$\nu_{\sigma,allB}$	1420405766 ± 17	14 ± 17	1420405762 ± 17	10 ± 17
$\nu_{\pi,smallB}$	1420405375 ± 42	-377 ± 42	1420405831 ± 74	79 ± 74
$\nu_{\pi,allB}$	142040569 ± 20	-62 ± 20	1420405908 ± 26	156 ± 26
Same B	1420405772 ± 15	20 ± 15	1420405772 ± 15	16 ± 15

From these data a weighted mean can be calculated for the σ-transition excluding the $\pm 4.398\,\mathrm{G}$ point resulting in

$$\text{Small B}: \ \nu_\sigma = (1420405767 \pm 13)\,\mathrm{Hz} \tag{6.2}$$

which deviates 15 Hz from the literature value with a relative precision of $9.2 \cdot 10^{-9}$. The corrected value for this transition is

$$\text{Small B corrected}: \ \nu_\sigma = (1420405757 \pm 14)\,\mathrm{Hz} \tag{6.3}$$

deviating 5 Hz from the literature value and having a relative precision of $9.9 \cdot 10^{-9}$.

The evaluation using all measured magnetic fields leads to a transition frequency for σ of

$$\text{All B} - \text{values}: \ \nu_\sigma = (1420405771 \pm 11)\,\mathrm{Hz} \tag{6.4}$$

which deviates 19 Hz from the literature value and has a relative precision of $7.7 \cdot 10^{-9}$. The correction gives a value of

$$\text{All B} - \text{values corrected } \nu_\sigma = (1420405768 \pm 11)\,\text{Hz} \tag{6.5}$$

which deviates 16 Hz from the literature value with a relative precision of $7.7 \cdot 10^{-9}$.

The uncorrected π-transition results can not be averaged because it reaches from -283 to -583 Hz which is an effect of the wrong theory used. The corrected value for the π-transition on the other hand can be calculated for the long term measurement to a value of

$$\text{Small B corrected : } \nu_\pi = (1420405827 \pm 52)\,\text{Hz} \tag{6.6}$$

which deviates 57 Hz from the literature value and has a relative precision of $36.6 \cdot 10^{-9}$. The same problem arises with the measured data at all magnetic field points. The corrected value of these is

$$\text{All B} - \text{values corrected : } \nu_\pi = (1420405917 \pm 18)\,\text{Hz} \tag{6.7}$$

deviating 165 Hz from the literature value with a relative precision of $12.7 \cdot 10^{-9}$.

Finally the three values for the transition frequency calculated by using the π- and σ-transition frequency at the same magnetic field can be averaged to a value of

$$\text{Same magnetic field : } \nu_0 = (1420405772 \pm 8)\,\text{Hz} \tag{6.8}$$

which deviates 20 Hz from the literature value having a relative precision of $5.6 \cdot 10^{-9}$ and for the corrected data

$$\text{Same magnetic field corrected : } \nu_0 = (1420405768 \pm 8)\,\text{Hz} \tag{6.9}$$

which deviates 16 Hz from the literature value and has a relative precision of $5.6 \cdot 10^{-9}$.

6.3 Discussion of the results

In table 6.5 the final results of the last two chapters are summarised. The reason for the splitting of the transition into small B and all B-values is because the October LT data are evaluated with and without the high magnetic field points generated by ± 1.9 A. "Small B" therefore means the evaluation of the transition frequency using only the magnetic field values produced by a current of ± 0.1 A, ± 0.06 A and ± 0.02 A while "All B-values" is the evaluation of all points of the October data respectively February data. "Same B" indicates the evaluation of the data done by using the central frequency of π and σ at the same static magnetic field.

Table 6.5: Difference of the final results of the transition frequencies from the literature value $\nu_{\text{lit}} = 1420405752\,\text{Hz}$.

Transition	**February (Hz)**		**October ST (Hz)**		**October LT1 (Hz)**		**OctoberLT2 (Hz)**	
	uncorr	corr	uncorr	corr	uncorr	corr	uncorr	corr
All B – values : ν_σ	6 ± 16	3 ± 25	–	–	22 ± 13	20 ± 13	14 ± 17	10 ± 17
Small B : ν_σ	–	–	14 ± 20	4 ± 21	10 ± 21	6 ± 21	12 ± 27	5 ± 27
All B – values : ν_π	-16 ± 23	61 ± 25	–	–	73 ± 20	172 ± 23	-62 ± 20	156 ± 26
Small B : ν_π	–	–	-583 ± 38	-99 ± 80	-283 ± 55	35 ± 73	-377 ± 42	79 ± 74
	uncorr	corr	uncorr		corr			
Same B : ν_0	4 ± 11	2 ± 11	20 ± 8		16 ± 8			

The uncorrected February data can be compared with the results in [8] done with MatLab (table 6.6). The results agree within the uncertainties.

Table 6.6: Comparison of the February results of this thesis and the results of [8]

Transition	Cuendis (Hz)	This thesis (Hz)
ν_σ	15 ± 15	6 ± 16
ν_π	8 ± 34	-16 ± 23
Mean value of the extrapolations	14 ± 14	-1 ± 14
Same B	1 ± 8	4 ± 11

The uncorrected October data show the shift at small magnetic fields described in the last chapter. Applying the correction, the values get shifted to higher frequencies. This can be explained by a residual magnetic field in y-z-direction. To look at the effect of this possible residual magnetic field on the σ-transition the extrapolation is done for the π-transition fixing the transition frequency to the ideal value. The magnetic field in y-z-direction is set as a parameter. The fit result of this residual field in y-z-direction is about $10^{-8} - 10^{-7}\,\text{T}$. For comparison the residual magnetic field in x-direction is a fit parameter in eq. 4.9 and is about $6 \cdot 10^{-7}\,\text{T}$. The resulting value is afterwards fixed for the σ-transition extrapolation. The residual magnetic field changes the σ-transition a few orders of magnitude less than the uncertainty and thus has no impact on the final result for the given precision.

Having a closer look on the results of the method using the transitions at same magnetic field it can be seen that the correction does not have a big effect. This comes from the fact that this method is independent of the magnetic field value as long as both transitions are measured at the same. As the correction is working with extracting the magnetic field value from the π-transition and afterwards calculating the theoretical value for the π- and σ-transition at this magnetic field it can differ from the uncorrected σ-transition. This difference changes the final result.

The σ-transition is not as sensitive as the π-transition on changes in the static magnetic field because of its hyperbolic shape. This leads to a lower effect of the correction which can be seen in the results.

Comparing the results of the October data evaluated with and without the $\pm 1.9\,\text{A}$ points the impact of these can be seen. At the π-transition the measured transition

frequency including the high magnetic field points suppress the shift to lower frequencies which arises at low magnetic fields. This is because the ± 1.9 A central frequencies can be obtained from the two-level system fit rather precisely and don't vary with changes in the magnetic field as much as the low magnetic field points. The extrapolation afterwards is quite fixed because of the precise measurement and therefore gives a result closer to the literature value. After the correction the results done with or without the ± 1.9 A respectively, the difference is about 2σ for the LT1 data and 1σ for the LT2 data. As this is a correction done after the evaluation of the data to look whether the shift could be explained with the four-level theory or not, and no fit, this deviation is acceptable.

In the case of the σ-transition the zero magnetic field transition frequency is in a region where the curve is quite flat. In this case the high magnetic field values and changes in the extrapolation fit don't have much impact on the value.

Chapter 7

Conclusion & Outlook

The hydrogen beam experiment was built as a supportive experiment of the ASACUSA antihydrogen experiment at CERN. The reason for building it was to test the spectrometer, i.e. the cavity and the sextupole magnets, for measuring the ground-state hyperfine splitting of antihydrogen. The same cavity characterised with hydrogen will be used in future experiments with antihydrogen to test the CPT symmtery. It was shown before that the cavity works as expected [8–10].

It was suggested in [8] to measure the central frequency at lower magnetic field to get more points in the region close to zero magnetic field, expecting a more precise result for the extrapolation. Not taking into account that the two-level system, used for previous evaluation, is not valid in this region anymore, the result shifted from the literature value and was investigated in this work. The evaluation gets more complex at low magnetic field because the splitting of the energy levels get narrower and it can not be regarded as a two-level system anymore. Attempting to correct the systematic effect caused by applying the two-level fit function in a regime where it stops being valid, it can be seen that the results are shifted towards the literature value at small magnetic fields.

In fig. 7.1 the uncertainty introduced by the correction as a function of the static magnetic field value is shown for the π-transition. The Error is calculated with a modification of eq. 5.10 (see chapter 5) as

$$\sigma_{\text{shift}} = \sqrt{\sigma^2_{\text{fake fit}} + \sigma^2_{\Delta B} + \sigma^2_{\Delta v}}. \tag{7.1}$$

Going to lower magnetic field values would increase the error bar significantly. At low magnetic field, the π-transition gets deformed and is therefore strongly dependent on the oscillating magnetic field value. As the uncertainty on the central frequency extracted by the two-level fit becomes a function of B_{osc}, the error gets bigger as small shifts in the oscillating magnetic field value will lead to a different central frequency (see fig. 5.1). So even using a four-level system will increase the error at small magnetic

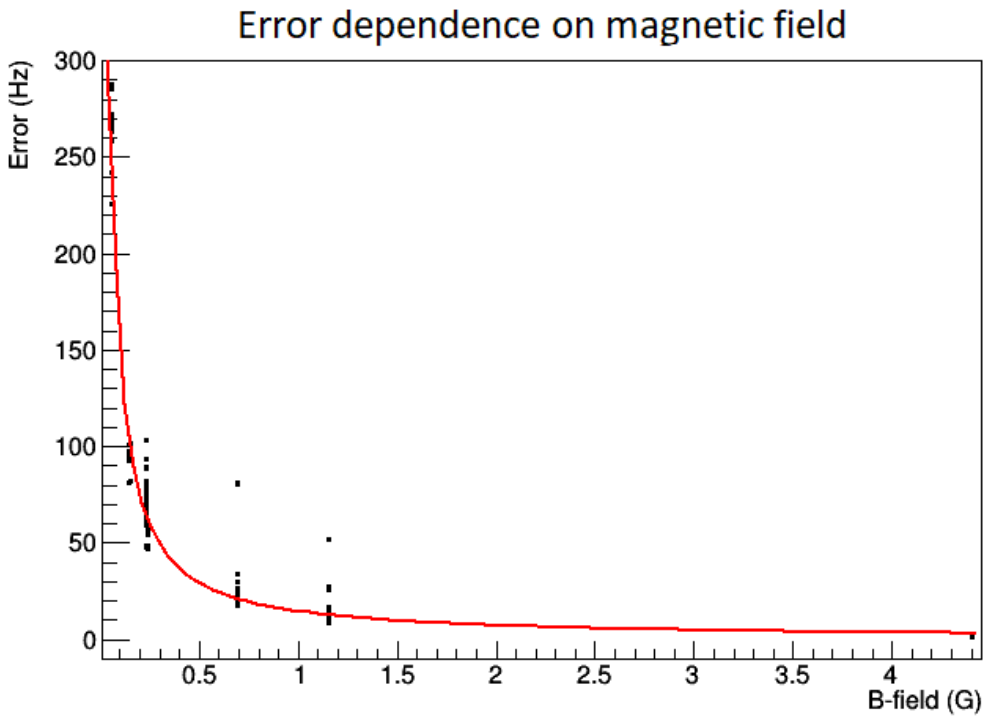

Figure 7.1: Dependency of the four-level uncertainty on the static magnetic field. The red curve is a fit function $\frac{A}{x} + b$. The values for the errors are calculated by using the oscillating B-field and velocity uncertainties of the real data.

field values unless the oscillating magnetic field can be determined independently with small uncertainty.

A further question is whether measuring the central frequencies at high static magnetic field values, and avoiding the region where the shift happens, would lead to a more precise result? A sketch of the extrapolation is shown in fig. 7.2 illustrating the relations of the uncertainties and static magnetic field values of the datapoints.

The error at zero-field depends on the uncertainty on the slope. This can be calculated for fig. 7.2 by having the distance of $2\Delta B$ between the second and third point (the spacing of $2\Delta B$ is chosen for the illustration because it is the spacing used for the measurement. In February $\Delta A = 0.1\,\mathrm{A}$: $0.1\,\mathrm{A}$, $0.3\,\mathrm{A}$, $0.5\,\mathrm{A}$; in October at small magnetic field $\Delta A = 0.02\,\mathrm{A}$: $0.02\,\mathrm{A}$, $0.06\,\mathrm{A}$, $0.1\,\mathrm{A}$)to

$$\Delta\nu_0 = \frac{2\Delta\nu_i}{4\Delta B} 3\Delta B \,, \tag{7.2}$$

where $\Delta\nu_0$ is the error of the zero-field transition frequency and $\Delta\nu_i$ is the error of the central frequency, which is the transition frequency at a certain magnetic field value. The uncertainty of the zero-field transition frequency is independent of the static magnetic field. The only dependency is on the proportion of the distance between

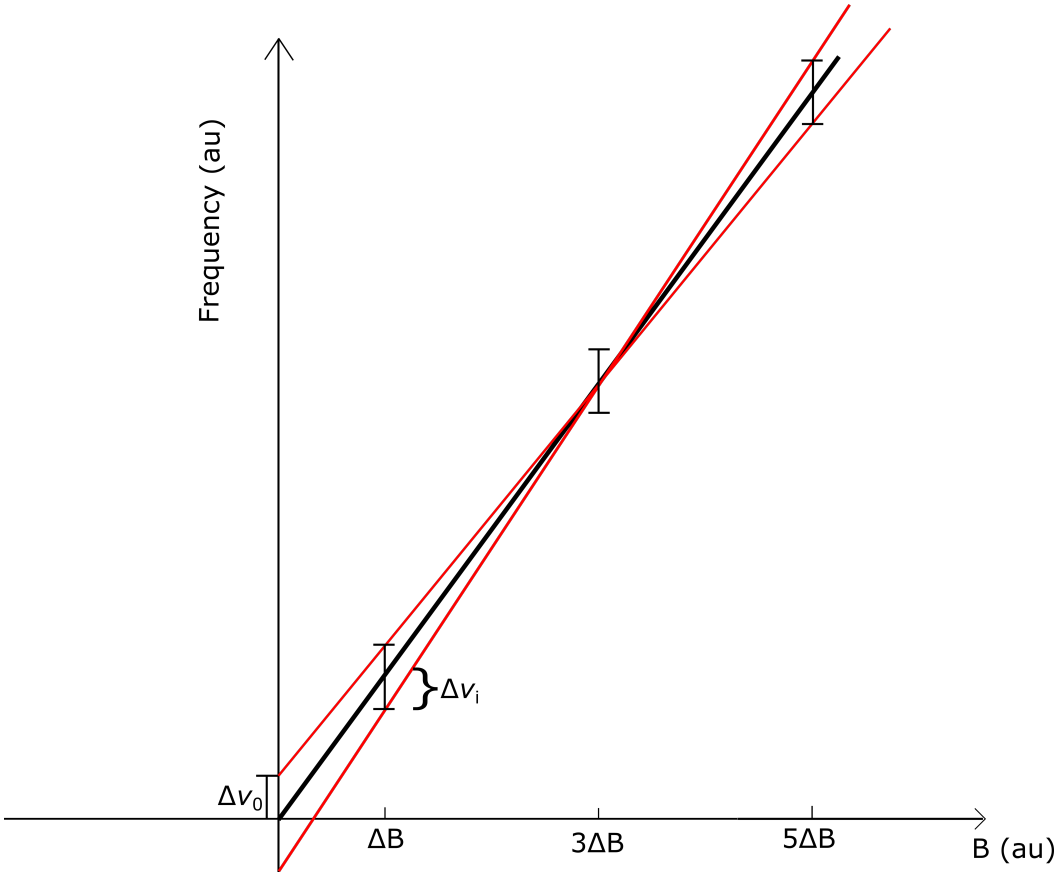

Figure 7.2: Sketch to illustrate the error of the zero-field hyperfine transition frequency $\Delta\nu_0$. The red curves are the boundaries of the extrapolation, the black curve is the optimum. The points and the errors $\Delta\nu_i$ are chosen arbitrarily.

the measured points. The lowest magnetic field value can be chosen rather arbitrarily (going too close to the zero-magnetic field region should still be avoided as the oscillating magnetic field dependency gets higher and therefore the uncertainty increases again). The result gets more precisely by having a bigger lever, i.e. a longer distance between the two points at higher magnetic field.

For the antihydrogen experiment there are four important conclusions from the results of this thesis:

- The method evaluating the data of π- and σ-transition simultaneously at the same magnetic field: This method is the most precise one investigated in this work and has the advantage of being independent of the static magnetic field value. It would be better to use it in a higher magnetic field region to avoid the impact of small changes of it but is also quite accurate at lower magnetic fields. It is the method of choice for starting spectroscopy on $\overline{\mathrm{H}}$ as two transitions are sufficient to calculate the zero-field splitting in a SME-sensitive way. The observed shifts are acceptable for $\overline{\mathrm{H}}$ as the first stage goal is a measurement with 1 kHz absolute precision.

- The 45 ° angle between the static and oscillating magnetic field should be avoided. It would be better to choose either orthogonal for the σ-transition and start a measurement and switch it to parallel for the π-measurement. This way the interaction of the different states of interest will vanish.

- Fit the data with a line-shape accounting for the four-level system. The advantage is that a large systematic error is avoided by including the complete physics. The disadvantage is that it will increase the time for the evaluation or the required computing power as solving the density matrix formalism for the four-level system is quite time-consuming and has to be done much more often if implemented on the level of the fit algorithm.

- Measure even at higher magnetic field values, for example the $\pm 2\,\mathrm{A}$ coil current generating the smallest magnetic field, going up to $\pm 10\,\mathrm{A}$. This has of course the advantage of avoiding the region of the small magnetic field shift and therefore can be solved using a two-level system which saves time.

Last but not least to get a better result it would be of interest to measure the static magnetic field in the cavity and not only the electric current. Knowing the value one can try to compensate possible residual magnetic fields.

The hydrogen experiment showed the functionality of the spin flip cavity and so lays the foundation for the ground-state hyperfine splitting measurement for antihydrogen. This in turn is a promising test of the CPT theorem and will help to extend our understanding of fundamental physics.

Chapter 8

Appendix

Appendix A: List of constants

Table 8.1: List of constants used in this thesis. From [30]

Name	Symbol	Value (SI)	Value (natural units)
Speed of light	c	$2.99792458 \cdot 10^8 \frac{\mathrm{m}}{\mathrm{s}}$	1
Planck constant	h	$6.626070040(81) \cdot 10^{-34}\,\mathrm{Js}$	$4.1356676 \cdot 10^{-15}\,\mathrm{eVs}$
Electron mass	m_e	$9.10938356(11) \cdot 10^{-31}\,\mathrm{kg}$	$0.5109989461(31)\,\mathrm{MeV}$
Proton mass	m_P	$1.672621898(21) \cdot 10^{-27}\,\mathrm{kg}$	$938.2720813(58)\,\mathrm{MeV}$
Bohr magneton	μ_B	$9.274009994(57) \cdot 10^{-24}\,\mathrm{J/T}$	$5.7883818012(26) \cdot 10 - 5\,\frac{\mathrm{eV}}{\mathrm{T}}$
Fine structure constant	α	$7.2973525664(17) \cdot 10^{-3}$	$7.2973525664(17) \cdot 10^{-3}$
Electron g-factor	g_e	$-2.00231930436182(52)$	$-2.00231930436182(52)$
Proton g-factor	g_P	5.585694702(17)	5.585694702(17)

Appendix B: Results of all sets

Table 8.2: Transition frequencies of each set of the February data (1-27) and October ST data (28-31)

Set	Uncorrected ν_σ (Hz)	Corrected ν_σ (Hz)	Uncorrected ν_π (Hz)	Corrected ν_{pi} (Hz)
1	1420405756 ± 68	1420405755 ± 68	1420405770 ± 95	1420405835 ± 100
2	1420405779 ± 63	1420405775 ± 63	1420405698 ± 90	1420405772 ± 97
3	1420405723 ± 65	1420405722 ± 65	1420405667 ± 95	1420405773 ± 105
4	1420405784 ± 66	1420405783 ± 66	1420405754 ± 97	1420405825 ± 105
5	1420405821 ± 71	1420405817 ± 71	1420405834 ± 105	1420405909 ± 113
6	1420405840 ± 69	1420405838 ± 70	1420405795 ± 108	1420405843 ± 112
7	1420405757 ± 78	1420405755 ± 80	1420405728 ± 119	1420405812 ± 126
8	1420405726 ± 75	1420405722 ± 75	1420405745 ± 118	1420405808 ± 122
9	1420405744 ± 76	142040574 ± 74	1420405602 ± 115	1420405677 ± 121
10	1420405799 ± 76	1420405795 ± 76	1420405766 ± 123	1420405835 ± 128
11	1420405746 ± 79	1420405744 ± 82	1420405702 ± 122	1420405790 ± 128
12	1420405800 ± 88	1420405796 ± 85	1420405909 ± 137	1420405994 ± 145
13	1420405704 ± 93	1420405670 ± 89	1420405802 ± 143	1420405863 ± 147
14	1420405750 ± 86	142040575 ± 83	1420405669 ± 125	1420405767 ± 131
15	1420405680 ± 81	1420405676 ± 83	1420405772 ± 119	1420405850 ± 126
16	1420405784 ± 80	1420405781 ± 80	1420405768 ± 121	1420405842 ± 166
17	1420405700 ± 75	1420405694 ± 75	1420405705 ± 107	1420405790 ± 115
18	1420405736 ± 79	1420405732 ± 71	1420405868 ± 119	1420405940 ± 125
19	1420405734 ± 71	1420405731 ± 71	1420405773 ± 101	1420405840 ± 106
20	1420405674 ± 75	1420405672 ± 75	1420405795 ± 112	1420405870 ± 118
21	1420405796 ± 82	1420405793 ± 82	1420405674 ± 122	1420405748 ± 128
22	1420405756 ± 86	1420405754 ± 85	1420405644 ± 118	1420405718 ± 123
23	1420405885 ± 93	1420405880 ± 97	1420405612 ± 148	1420405690 ± 153
24	1420405681 ± 96	1420405678 ± 99	1420405880 ± 97	1420405754 ± 147
25	1420405770 ± 101	1420405767 ± 101	1420405745 ± 141	1420405850 ± 149
26	1420405784 ± 103	1420405775 ± 103	1420405669 ± 154	1420405776 ± 163
27	1420405751 ± 117	1420405751 ± 113	1420405619 ± 162	1420405727 ± 170

Table 8.3: Transition frequencies of each set of the October ST data

Set	Uncorrected ν_σ (Hz)	Corrected ν_σ (Hz)	Uncorrected ν_π (Hz)	Corrected ν_{pi} (Hz)
1	1420405753 ± 39	1420405745 ± 38	1420405157 ± 72	1420405603 ± 147
2	1420405810 ± 40	1420405801 ± 40	1420405292 ± 83	1420405826 ± 167
3	1420405750 ± 42	1420405740 ± 43	1420405143 ± 75	1420405579 ± 163
4	1420405746 ± 41	1420405735 ± 42	1420405106 ± 75	1420405624 ± 159

Table 8.4: Transition frequencies calculated with all magnetic field values for October LT data

Set	Uncorrected ν_σ (Hz)	Corrected ν_σ (Hz)	Uncorrected ν_π (Hz)	Corrected ν_{pi} (Hz)
1	1420405759 ± 29	1420405757 ± 29	1420405838 ± 45	1420405941 ± 54
2	1420405790 ± 29	1420405786 ± 29	1420405939 ± 50	1420406046 ± 59
3	1420405796 ± 31	1420405794 ± 31	1420405808 ± 46	1420405897 ± 53
4	1420405759 ± 32	1420405757 ± 32	1420405844 ± 47	1420405974 ± 56
5	1420405763 ± 34	1420405760 ± 34	1420405707 ± 50	1420405782 ± 56
6	1420405778 ± 40	1420405775 ± 40	1420405803 ± 59	1420405914 ± 67
7	1420405761 ± 35	1420405757 ± 35	1420405639 ± 41	1420405829 ± 63
8	1420405743 ± 37	1420405739 ± 37	1420405748 ± 45	1420405998 ± 59
9	1420405792 ± 40	1420405787 ± 40	1420405620 ± 47	1420405867 ± 61
10	1420405776 ± 44	1420405773 ± 44	1420405732 ± 52	1420405928 ± 66
11	1420405777 ± 49	1420405772 ± 48	1420405738 ± 59	1420405951 ± 74
12	1420405747 ± 53	1420405743 ± 52	1420405711 ± 62	1420405902 ± 75

Table 8.5: Transition frequencies calculated with small magnetic field values for October LT data

Set	Uncorrected ν_σ (Hz)	Corrected ν_σ (Hz)	Uncorrected ν_π (Hz)	Corrected ν_{pi} (Hz)
1	1420405757 ± 53	1420405753 ± 51	1420405337 ± 127	1420405684 ± 198
2	1420405761 ± 50	1420405756 ± 52	1420405404 ± 146	1420405779 ± 210
3	1420405773 ± 49	1420405771 ± 49	1420405529 ± 121	1420405784 ± 159
4	1420405735 ± 49	1420405732 ± 49	1420405391 ± 129	1420405756 ± 166
5	1420405730 ± 53	1420405726 ± 53	1420405566 ± 131	1420405778 ± 154
6	1420405817 ± 54	1420405814 ± 53	1420405608 ± 150	1420405986 ± 214
7	1420405748 ± 54	1420405741 ± 55	1420405366 ± 89	1420405771 ± 154
8	1420405727 ± 58	1420405722 ± 57	1420405340 ± 92	1420405827 ± 174
9	1420405799 ± 61	1420405790 ± 62	1420405242 ± 98	1420405760 ± 177
10	1420405822 ± 67	1420405817 ± 68	1420405455 ± 106	1420405841 ± 184
11	1420405756 ± 78	1420405749 ± 77	1420405459 ± 116	1420405939 ± 204
12	1420405731 ± 81	1420405725 ± 83	1420405474 ± 129	1420405916 ± 206

Bibliography

[1] P. Dirac, M. Adrien and R. H. Fowler. A theory of electrons and protons. *Proc. R. Soc. Lond. A.*

[2] C. D. Anderson. The positive electron. *Phys. Rev.*, 43:491–494, Mar 1933.

[3] G. Baur, G. Boero et al. Production of antihydrogen. *Physics Letters B*, 368(3):251 – 258, 1996.

[4] E. Widmann et. al. Hyperfine structure measurements of antiprotonic helium and antihydrogen. In *Lecture Notes in Physics 570, 528.*

[5] B. Kolbinger. Numerical simulations of hyperfine transitions in antihydrogen. Master's thesis, University of Vienna, 2014.

[6] N. Kuroda et al. A source of antihydrogen for in-flight hyperfine spectroscopy. *Nat. Commun.*, 5, 2014.

[7] D. Colladay and A. V. Kostelecký. Lorentz-violating extension of the standard model. *Phys. Rev. D*, 58:116002, 1998.

[8] S. Argueda Cuendis. Measuring the hydrogen ground state hyperfine splitting through the π_1 and σ_1 transitions. Master's thesis, University of Vienna, 2017.

[9] M. Wiesinger. Design and Implementation of New Optics for the Atomic Hydrogen Beam of ASACUSA's Antihydrogen Hyperfine Spectroscopy Experiment. Master's thesis, University of Technology Vienna, Feb. 2017.

[10] M. Diermaier. *Determination of the Hydrogen Ground-State Hyperfine Splitting in a Beam and Perspectives for Antihydrogen.* PhD thesis, Technical University of Vienna, 2016.

[11] C. S. Wu et al. Experimental test of parity conservation in beta decay. *Phys. Rev.*, 105:1413–1415, Feb 1957.

[12] J. H. Christenson, J. W. Cronin, V. L. Fitch and R. Turlay. Evidence for the 2π decay of the k_2^0 meson. *Phys. Rev. Lett.*, 13:138–140, Jul 1964.

[13] R.F. Streater and A. S. Wightman. *PCT, spin and statistics, and all that.* Princeton landmarks in physics. Princeton, NJ, 2000.

[14] D. H. Perkins. *Introduction to High Energy Physics.* Cambridge University Press, Cambridge, 2000.

[15] N. Bohr. On the Constitution of Atoms and Molecules, Part I. *Philosophical Magazine*, 26:1–25, 1913.

[16] H. Friedrich. *Theoretical Atomic Physics.* Springer, Berlin [u.a.], 1991.

[17] Freeman Dyson. *Dyson Quantenfeldtheorie: Die weltbekannte Einführung von einem der Väter der QED.* Springer, Berlin Heidelberg, 2014.

[18] R. P. Feynman. *The Feynman lectures on physics 3: Quantum mechanics.* Addison-Wesley, Reading, Mass. [u.a.], 2. print. edition, 1965.

[19] R. Loudon. *The quantum theory of light.* Oxford science publications. Oxford University Press, Oxford, 3. ed. edition, 2000.

[20] A. V. Kostelecký and A. J. Vargas. Lorentz and CPT tests with hydrogen, antihydrogen, and related systems. *Phys. Rev.*, D92(5):056002, 2015.

[21] M. A. Humphrey et al. Testing cpt and lorentz symmetry with hydrogen masers. *Phys. Rev. A*, 68:063807, Dec 2003.

[22] I. I. Rabi, S. Millman, P. Kusch and J. R. Zacharias. The molecular beam resonance method for measuring nuclear magnetic moments. the magnetic moments of ${}_3\mathrm{Li}^6$, ${}_3\mathrm{Li}^7$ and ${}_9\mathrm{F}^{19}$. *Phys. Rev.*, 55:526–535, Mar 1939.

[23] C. Malbrunot et al. A hydrogen beam to characterize the asacusa antihydrogen hyperfine spectrometer. *Nuclear Instruments and Methods in Physics Research Section A: Accelerators, Spectrometers, Detectors and Associated Equipment*, 935:110 – 120, 2019.

[24] M. Wolf. Lock-in based detection scheme for a hydrogen beam. Master's thesis, University of Vienna, 2013.

[25] S. Federmann. *A Spin-Flip Cavity for Microwave Spectroscopy of Antihydrogen.* PhD thesis, University of Vienna, 2012.

[26] B. Juhász and E. Wiedmann. Planned measurement of the ground-state hyperfine splitting of antihydrogen. *Hyperfine Interact*, 193:305–311, Aug 2009.

[27] L. W. McKeehan. Combination of Circular Currents for Producing Uniform Magnetic Fields. *Review of Scientific Instruments*, 7:150, 1936.

[28] C. B. Jepsen. Data Taking and Simulation-Based Data Analysis at the ASACUSA Experiment. CERN summer student work project report:, 2014. http://cds.cern.ch/record/1752579.

[29] C. Sauerzopf. *The ASACUSA Antihydrogen Detector: Development and Data Analysis* . PhD thesis, University of Technology Vienna, 2016.

[30] P. J. Mohr, D. B. Newell and B. N. Taylor. CODATA recommended values of the fundamental physical constants: 2014. *Reviews of modern Physics*, 88, 2016.